Politecnico di Torino

Politecnico di Torino

MSc Mechanical Engineering

A.y. 2025-2026

Graduation Session July 2026

Numerical study and design exploration of a PCM-based cold thermal energy storage device for Data Centers

Supervisors:	Candidate:
Eliodoro Chiavazzo	Mario Rosario De Angelis
Matteo Morciano	

Table of Contents

Chapter 1

Introduction

1.1 PCMs and Thermal Management

1.1.1 Applications

Phase Change Materials (PCM) are currently in the spotlight as solutions for **thermal management** and **thermal energy storage** for various types of device.

PCMs have been adopted to mitigate thermal shock in high heat flux components (such as CPUs) achieving higher longevity and a volume reduction for traditionally used heatsinks. At the same time a similar effect was achieved for Photovoltaic Panels (PVs) allowing for uninterrupted 24 hours electrical energy generation. Similarly, Lithium Ion Batteries (LIBs) for Electrical Vehicles (EVs) are a similar management challenge as thermal runaway is a common problem, especially under high discharge rates yet PCMs were succesfully utilized to improve efficiency and power delivery. Additionally, special types of fabric were developed with encapsulated PCM to improve thermal comfort by both absorbing endogenous heat and by providing a cooling effect when possible thus reducing the need for AC.
PCMs have also been employed as thermal batteries to improve operational stability in Solar Thermal Collectors (SCTs) by storing excess energy during peak hours in order to further extend operation. Similarly they were succesfully designed to aid in extended and efficient operation of Solar Desalization devices by storing excess solar energy in order to extend the evaporation process beyond peak hours. With proper design PCMs are capable of providing a boost in performance for Building Envelopes by acting as thermal inertia masses thus improving both energy expenditures and thermal comfort [1].
Numerical models and CFD simulations have been used to analyze and confirm PCM based thermal management and thermal energy storage devices' capabilities [2] [3].
Mo et al. [4] employed a thermal regulation system that is capable of managing

peak load cooling and battery pre-heating. They conclude that with proper design and adaptation PCM batteries are adaptable to "All-Climate" conditions. Ge et al. [5] employed a paraffin composite along with a serpentine heat exchanger design as a solution for the thermal management of a cylindrical battery pack. Their work focused not only on thermal management but also on the improvement of thermal contact showing that material choice and design is a key component in the design process . Chen et al. [6] designed a device with adjustable fins used for the discharging process. Their solution employs movable fins to induce motion in the molten PCM to sensibly improve heat transfer.

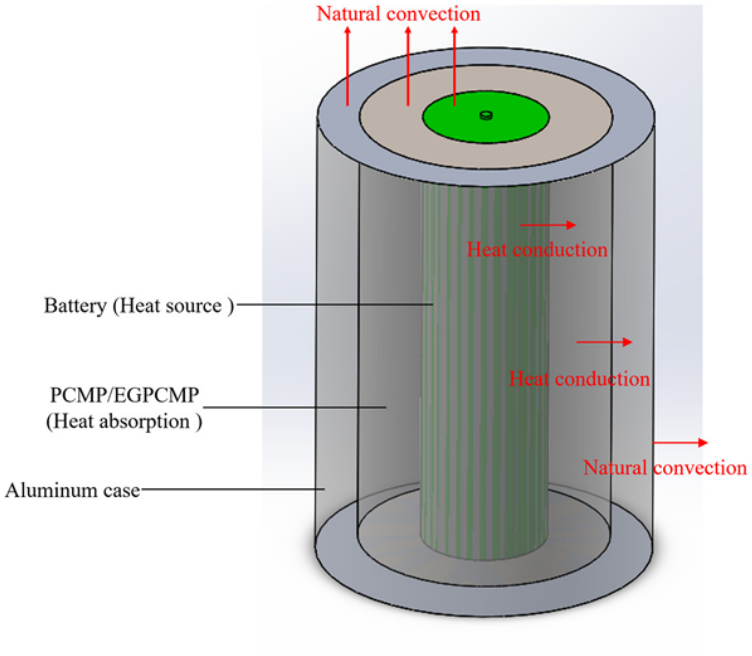

Figure 1.1: Example of a PCM Based Battery Thermal Management Unit. Source: Chen et al. [7].

The cited works are not exhaustive but they show different design aspects that are key for PCM based thermal batteries:

1. Geometry
2. Heat Transfer
3. Material Choice

A promising new application is that of **Data Centers (DCs)** for which, at the time of writing, research is still relatively novel.

1.1.2 Working Principles

The operating principle of PCM-based thermal batteries relies on **the exploitation of phase change and latent heat storage for thermal regulation**. Phase change materials (PCMs) undergo a phase transition within a specific temperature range, which represents a key parameter in determining their suitability for a given application [8] [9]. During the phase transition, PCMs absorb or release large amounts of latent heat while maintaining nearly constant temperature. This behavior provides **high thermal inertia** and enables effective thermal management. As thermal batteries, PCMs undergo charging and discharging cycles in which thermal energy is respectively stored and released. The thermophysical behavior of PCMs differs between these two processes due to changes in the dominant heat transfer mechanisms and phase distribution, requiring **dedicated analysis of both charging and discharging conditions** [10] [11].
Despite their advantages, PCM-based thermal batteries face several technological challenges, including:

1. Poor Thermal Conductivity of PCMs.
2. Efficient recharging of the PCM after discharge.

Literature has a plethora of articles focused on **mitigation of poor conductivity** in phase change materials. Yuan et al. [12] show that by incorporating PCM into highly conductive expanded graphite 3D structures overall conductivity increases up to 5 times. Similarly, Dhabarbe et al. [13] investigated the effects of metal foams with varying porosities in conjunction with geometrical optimization (external honeycomb structures) to improve both conductivity and melting performance. On the other hand Singh et al. [14] investigated possible improvements derived from different nanoparticle solutions such as multi-walled carbon nanotubes, graphene and carbon fiber. They show that compared to the standard control PCM cell temperature up to a certain time is drastically reduced.

Charging processes are to be tailored to each case and often they require a secondary heating/cooling system to achieve restoration of PCMs. Gungor et al. [15] suggest the use of an alternative cooling solution for the charging of the PCM device analyzing the process as an "in-between" working cycles condition. Khumar et al. [2] employed a hybrid PCM system where the active component of the system was used to restore molten PCM to a solid phase.

The literature indicates that **peak shaving** is one of the most promising applications of PCM-based thermal batteries. This aspect has been investigated in the works of Morciano et al. [1] , Khumar et al. [2] and several other studies that will be reviewed and discussed throughout this thesis.

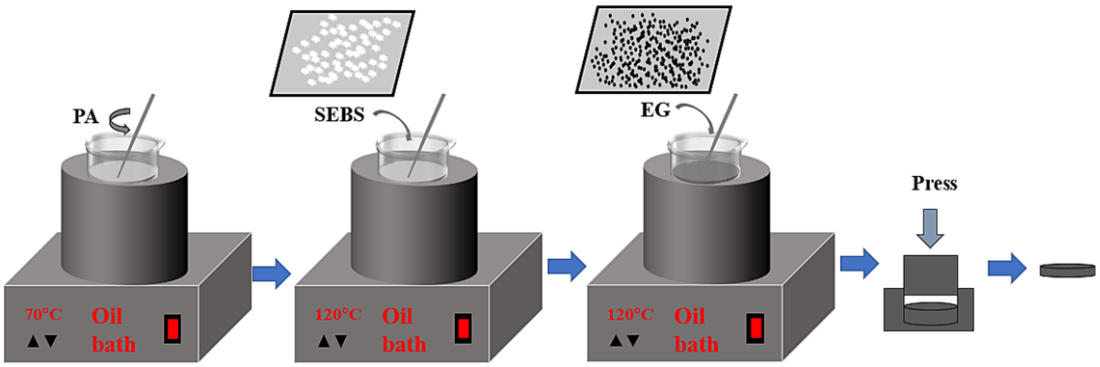

Figure 1.2: Preparation of a hybrid PCM structure with expanded graphite. Source: Yuan et al. [12].

1.2 State of the Art and Current Trends

PCMs have been extensively investigated for lithium-ion battery thermal management in electric vehicles (EVs) with many applications showcasing their succesful use as a thermal regulation material. Paraffins have been shown to adapt well to temperature ranges required in those applications as demonstrated by Ammar et al. [16] who investigated the requirements that PCM based thermal batteries are to possess for EV-based applications while demonstrating the viability of a proposed solution through CFD simulations. Further compounding on the idea, Rana et al. [9] mention that no single paraffin can be considered universally optimal but they are to be adapted to the problem's boundary conditions. As discussed, the feasibility of PCM-based thermal management systems has been extensively investigated [1]. Research efforts have also focused on optimizing heat exchange for harsher discharge rates. Mohammed et al. [17] examined extreme discharge conditions (9C) while using non-paraffin based metallic PCM (GaPCM) showing that the solution space in terms of material choice is quite broad. The common line between all solutions is the ability of the thermal management systems to **quickly adapt and scale to different working conditions**, many of which are extreme in nature.

Design and studies benefit from empirical and numerical models to gain insights about possible system responses. This is a key factor in the study of novel technologies. As such, research efforts have addressed **thermal management optimization at multiple scales**, ranging from individual battery cells to full battery pack configurations. The scale difference results in different optimization routes and different CFD models (where applicable). The effect of different casing geometries, PCM modifications, and innovative thermal management strategies has been shown to mitigate the limitations associated with the low thermal conductivity

of PCMs. This line of study encompasses the idea of altering a PCM based device geometry to improve its performance, one of the key techniques in improvement processes for existing ideas and designs.
Soliman et al. [18] designed a novel single-battery casing that employs two different separate PCMs in the orthogonal casing fins combining two different heat dissipation mechanisms: casing and fins. Previously cited Singh et al. [14] designed and simulated "Z-shaped" fins made to favor heat transfer through Rayleigh–Bènard convection cells.
Design improvements have also focused on altering PCMs with high conductivity additives and/or the combined study of auxiliary systems with latent heat exchange mechanisms that characterize PCM devices.

Chen et al. [19] evaluated an impregnated PCM configuration with expanded graphite. They examined different expanded graphite mass fractions to pinpoint an optimum between thermal performance and material use.
Ammar et al. [16] analyzed and simulated a battery pack. The work focused on simulations and parametric sweeps to obtain data about the optimal parameters for the combined PCM and liquid cooling system.

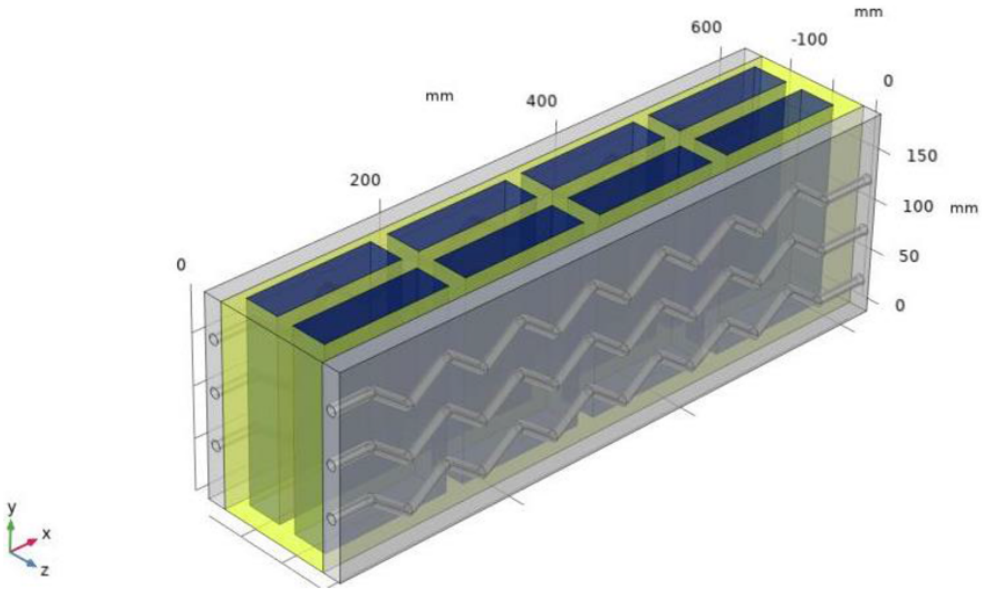

Figure 1.3: Hybrid Cold Plate and PCM Battery Cooling Solution using paraffin with EG as PCM. Source: Ammar et al. [16].

As implied before, **the growing interest in PCM-based battery thermal management has resulted in the availability of extensive experimental**

datasets for model development and validation. To model battery behaviour accurately domain-specific models and data are used. Sun et al. [20] have modelled heat release in batteries through the Bernardi equation which separates the total heat generation into reversible (entropic) and irreversible (Joule) contributions. On the other hand Sing et al. [14] used an empirical model based on lab data from Newman, Tiedemann Gu & Kim (NTGK) to reduce computational costs while achieving high accuracy.
It is clear that works on Li-Ion batteries benefit from models that express the relationship between characteristic working parameters and heat generated thus allowing authors to achieve great agreement with experimental data resulting in more accurate predictions and designs.

More broadly **PCM modelling** is often approached through some more common methods such as Enthalpy-Porosity or Apparent Specific Heat method. They belong to the "fixed domain" methods as they do not explicitly track the phase change front [21]. These methods generally provide good agreement with experimental observations while maintaining reasonable computational costs. The melting front is recognized as a critical component for design and deduction of information as the main site of the steepest thermal gradients and property changes but the approximation is often accepted as an accurate-enough solution [22].

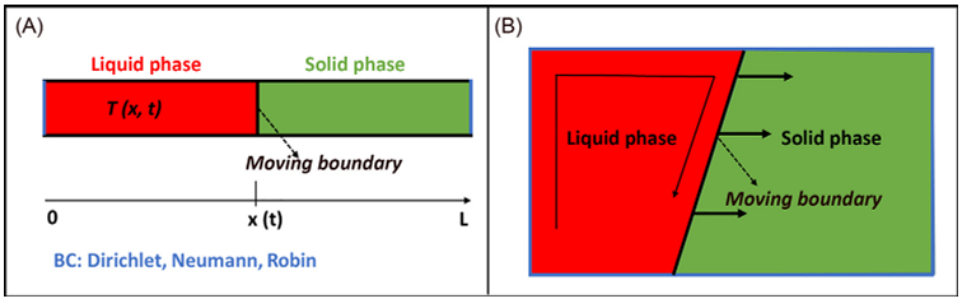

Figure 1.4: Schematic of a moving boundary phase change problem (Stefan problem). (A) represents a 1D problem, (B) represents a 2D problem. Source: Numerical methods for solid-liquid phase-change problems - Chapter 7 [21].

The previously cited availability of domain specific validated numerical models has enabled the adoption of advanced optimization methodologies, including **Topology Optimization (TO)**. Topology optimization has emerged as a promising design methodology in the optimization of heat exchange for PCM thermal management devices: the combination of modestly expensive models and data availability make

repeated optimization runs possible and feasible. Furthermore, additive manufacturing allows a broader scope of design especially in the prototyping space. This method builds on a wide gamut of already estabilished literature by proposing a mathematically driven optimization process that is an alternate route to more traditional design-space explorations offering interesting and otherwise challenging to reach insights.
Belwadi et al. [23] used the SIMP algorithm to design innovative fin shapes in which PCM is immersed for cylindrical battery cooling. Their topologically optimized design improved thermal gradient distribution and lowered peak battery temperature. Sun et al. [20] used topology optimization to design a novel liquid cooling channel used in conjunction with PCM to cool a battery pack. They propose different designs derived from an objective function that seeks to minimize pumping costs and peak battery temperature.

In stark contrast to all examples discussed, the application of PCM-based thermal batteries to **data center thermal management** remains relatively underexplored. The literature review conducted for this thesis identified only three studies investigating the use of PCMs for data center thermal management. The papers focus on emergency cooling and energy storage. They will be explored in the next chapter.

1.3 Data Centers

1.3.1 The emerging importance of Data Centers

Data centers are emerging as one of the most significant contributors to the growth of global electricity demand. With the rise of AI technologies as a main component of industrial and civil industrial and consumer applications their optimization and operation has become a leading line in research. The IEA estimates that approximately 15% of data center electricity consumption is currently associated with AI-related workloads [24]. The IEA also estimates that by the end of 2026 Data Center energy demands may spike over 1000 TWh due to the concurring effects of AI and Cryptomining [25]. Notably, 43% of data center capacity comes from the USA where the combined electricity consumption of facilities is estimated to account for 6% of national electricity demand by the end of 2026 [24] [25].
The rapid growth of AI services and data storage infrastructure is driving a **sustained increase in energy demand**. The one of interest for this work is that of **cooling load** which is often tied to electric power consumption. In particular, it is estimated that the cooling load accounts for 40% to 50% of the total energy cost in a data center [26] .

To maintain acceptable working conditions (and thus maximum efficiency of operating systems) hardware temperature needs to be controlled. To achieve the

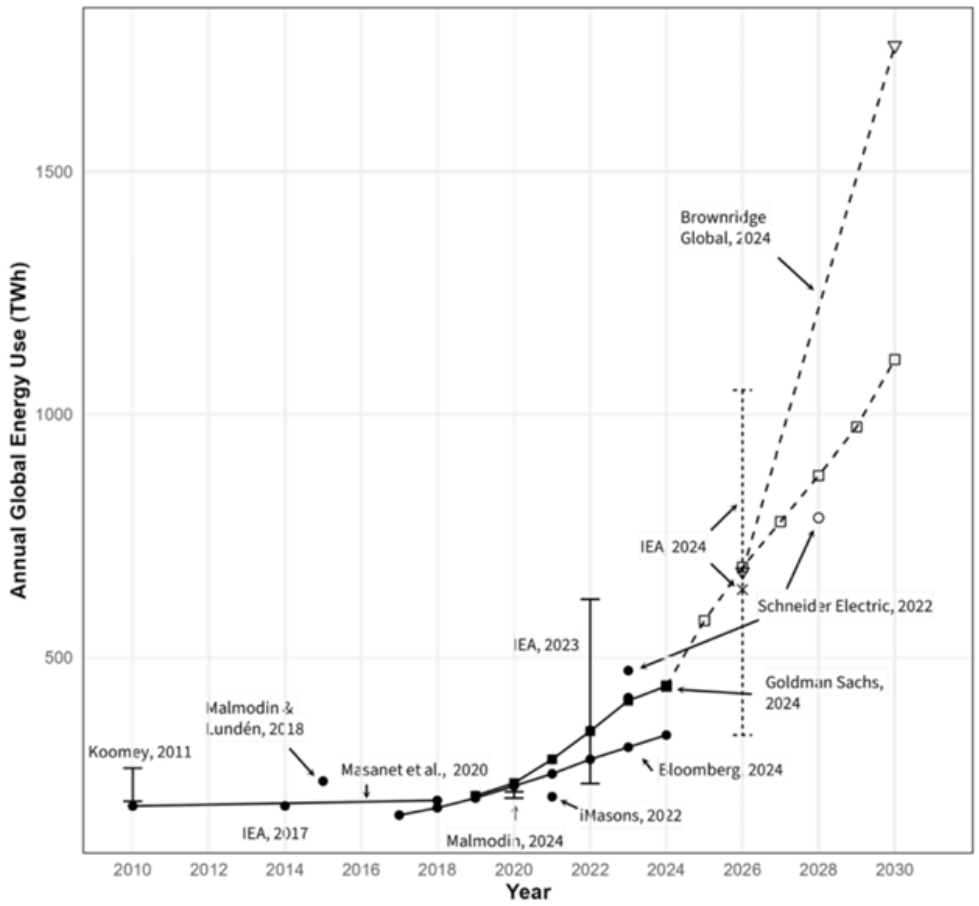

Figure 1.5: Global Data Center energy consumption estimates from academy and industry. Source: Kim et al. [26].

objective various solutions are explored and considered which are common to other fields of engineering. Two of the main solutions are **direct liquid cooling** in which a thermofluidic vector is used to remove heat from critical components and **immersion cooling** which is another emerging technology wherein hardware is totally immersed into a fluid allowing the removal of heat as it is generated [27]. These approaches act directly at the hardware level by removing heat from the computing components. In addition to component-level cooling, facility-level thermal management is required. The latter is often achieved through more traditional means which are broadly included in CRAC (Computer Room Air Conditioning). Components pertaining to this category are chillers, water pumps, cooling towers and fans [28].

Beyond thermal management technologies, significant research efforts have

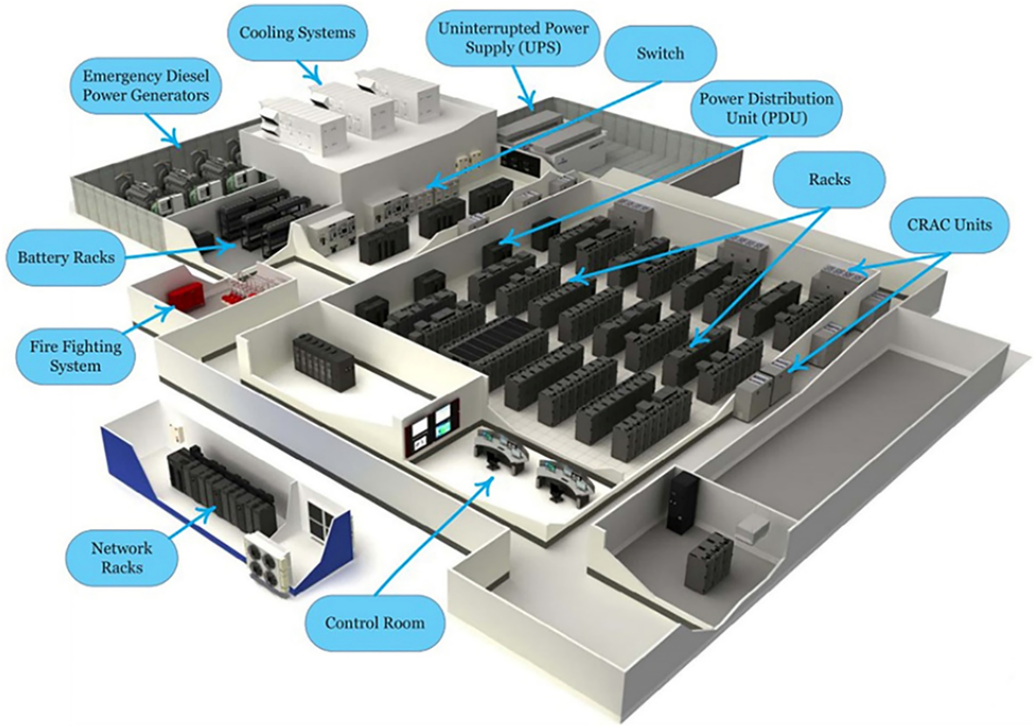

Figure 1.6: Schematic layout of a typical data center setup. Source: Yuan et al. [28].

focused on **system-level energy optimization strategies**. Kumar et al. [27] provide an overview of some methods:

1. Peak shaving through ESS (Energy Storage Systems)
2. Demand response
3. Workload shifting

Peak shaving through ESS consists in using energy accumulation systems during peak hours to reduce demand on the main energy grid. The accumulation systems are charged during off-peak hours to store energy purchased from the grid at a generally lower rate compared to peak hours.
Demand response consists in the dynamic re-allocation of some internal systems to assist and favour the local grid during peak hours, where possible.
Workload shifting consists in the temporal or spatial shifting of computing load. The former means that non-critical jobs are moved in time to favour urgent requests and the latter means that the computing load is re-distributed to data centers in

another location.

All of these strategies can potentially benefit from thermal energy storage technologies, including latent heat thermal batteries based on phase change materials. It is thus evident how the benefits reaped in other fields, as discussed, may be transposed to data centers. This is even more evident as argued by Kumar et al. [27]: due to the impossibility of adapting the electrical grid to increasing energy demands **optimizing on-site systems is likely to play a key role in mitigating these challenges in the near term**.

1.3.2 State of the art on Data Centers and PCM Cooling

For Data Centers **the use of PCM as a thermal battery is quite novel**. The literature review conducted for this thesis identified only a limited number of studies specifically addressing PCM-based thermal energy storage in data center applications.

Yuan et al. [12] propose an **encapsulated PCM as a thermal heatsink** for data center CPUs. They developed a composite material consisting of of PA, SEBS and EG resulting in a Flexible PCM (FPCM). The device is then directly attached on top of server casings to absorb heat coming from internal components. Their blend also results in a relatively high thermal conductivity (above 0.72 $[\frac{W}{mK}]$). They also propose different mass fractions for PCM and EG encapsulation to modulate thermal conductivity and phase change enthalpy. They model the system through Flotherm to simulate air flowing into a casing in which a CPU is present along with FPCM. They conclude that thanks to their FPCM heatsink it is possible to reduce cooling energy demand by up to 24.73% while significantly extending CPU service life.

Huang et al. [8] study a **PCM based cold energy storage tank** to aid traditional air cooling in emergency situations. The device consists of parallel rectangular PCM plates arranged in parallel with incoming air from the air conditioning unit. As air passes through the device and makes contact with the plates containing the PCM (eutectic fatty acid) it loses heat thus lowering its temperature. An arcuate version of the device is also proposed to enhance heat transfer between air and the plates containing PCM. Heat exchange with hot air then serves as a mean to keep ambient temperature below the maximum allowed. By specifying a criterion to meet for emergency conditions (maintaining the outlet air temperature below 27 °C) they show that the PCM based solution is effectively able to meet the requirements up to 300s while the geometrically improved arcuate solution worked up until 900s across a wide spectrum of boundary conditions underlining

the importance of geometrically altering simple designs to improve starting point baselines.

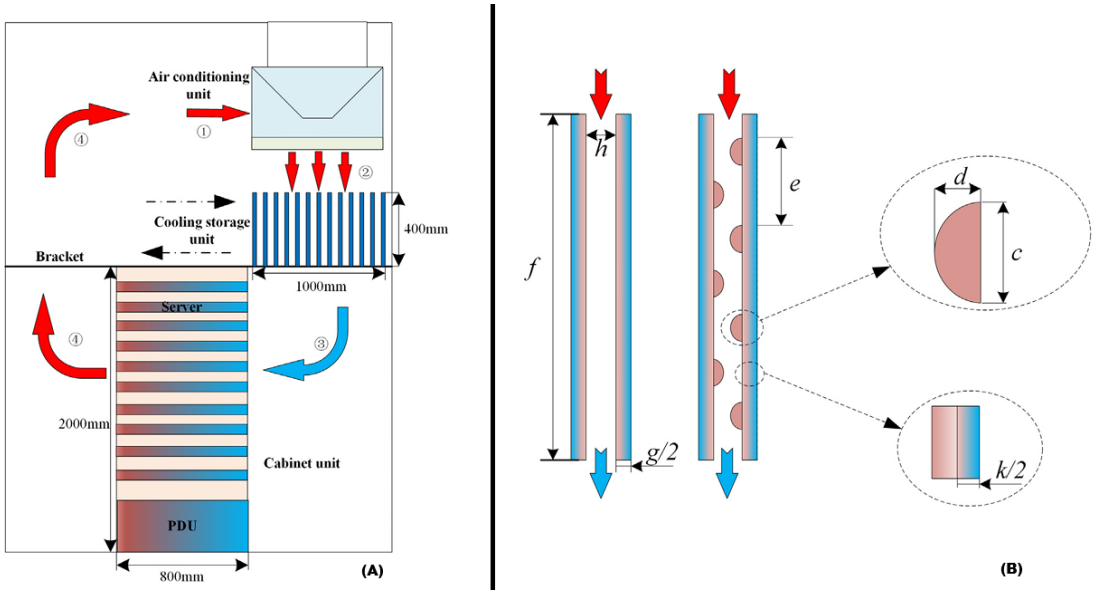

Figure 1.7: PCM based cold energy storage for emergency air conditioning. (A) is the general schematic layout of the system, (B) represents the nominal and optimized airflow channel designs. Source: Huang et al. [8].

Liang et al. [11] focus on a **water to PCM heat exchanger** where PCM is contained in rectangular HDPE plates arranged perpendicularly to the direction of water, forming different flow channels. They perform a preliminary study on a smaller scale by collecting experimental data and modelling their test platform on ANSYS through the apparent specific heat method. They propose a framework of improvement on the base design by adding internal fins to the PCM plates and using response surface methodology to optimize the device. The results are then succesfully scaled to real life case studies showing how modelling and validating at a lower scale may be a mean of optimizing for more general use-cases. They show how in the real world the improved configuration achieves utilization rates up to 18.3% more than the base configuration.

Building upon the work of Liang et al. [11] , this thesis develops an alternative numerical framework based on the enthalpy-porosity method. Compared to the original approach, the proposed model aims to reduce computational complexity while retaining sufficient accuracy for design optimization studies by exploiting the

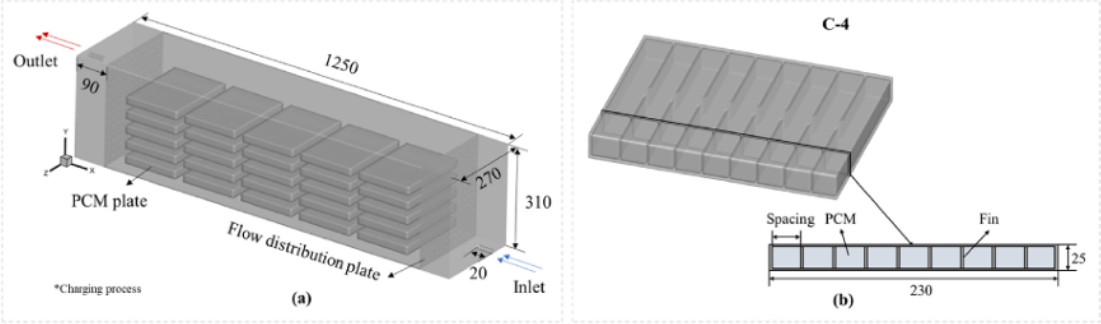

Figure 1.8: 3D Schematic of a PCM based cold thermal energy storage for water. (a) is the overall device schematic, (b) is schematic of the internal structure used by Liang et al. to optimize heat exchange. Source: Liang et al. [11].

method's modularity in terms of modelling choices [21]. This enables the investigation of a broader design space and facilitates the application of optimization methodologies at both the component and system levels. In addition, a novel optimization strategy based on **hotspot density** is proposed to address the thermal limitations imposed by the low conductivity of HDPE encapsulation plates.

Chapter 2

Numerical Model and Validation

2.1 Experimental Setup and Material Data

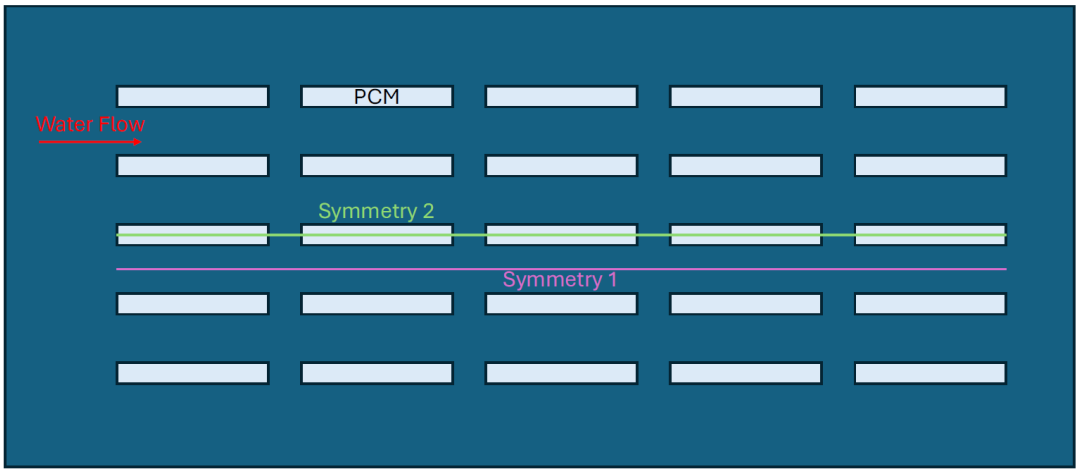

Figure 2.1: Schematic of simulation domain.

The testing platform setup by Liang et al. consists of an enclosure with 25 PCM containment plates. Hot water flows in the device at a rate of $6.33 \cdot 10^{-5}$ $\frac{m^3}{s}$ through a cylindrical channel with $D = 12.7$ mm. A perforated distribution plate homogenizes flow through the apparatus resulting in a Reynolds Number of $Re = 55$ calculated in respect to the average elementary channel velocity. The average inlet velocity in each single rectangular channel is $v_w = 0.0012$ $\frac{m}{s}$ which produces a

maximum striction velocity in simulations of about 0.04 $\frac{m}{s}$ in agreement with Liang et al. who observe maximum device velocity of $v_w = 0.05\ \frac{m}{s}$. The device is shown in figure 1.8 and for this work the version without fins will be considered for validation, as done by the original authors.

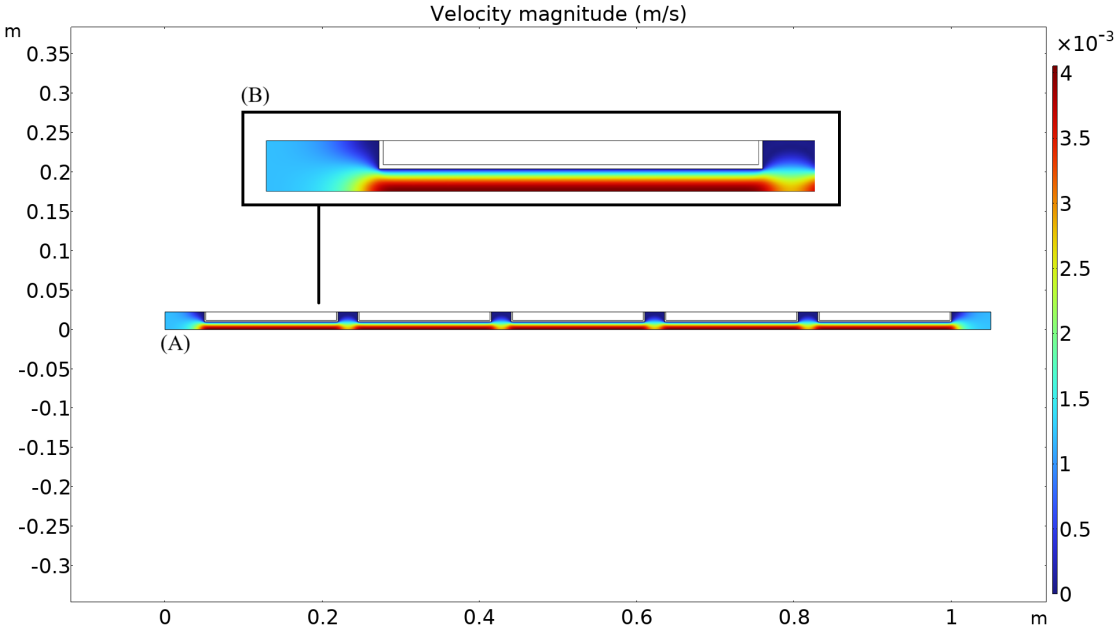

Figure 2.2: Water velocity field. (A) is the overall view, (B) represents a detail view.

Through conductive and convective heat transfer the PCM absorbs heat from the water thus functioning as **cold thermal energy storage** (discharging process). The PCM material chosen by Liang et al. is a salt hydrate, PCM8, while the plating consists of HDPE. Material properties are shown in the following table. Specific heat for PCM8 will be calculated in different ways in the following pages.

	PCM8	HDPE
Thermal Conductivity $[\frac{W}{mK}]$	0.6837	0.24
Density $[\frac{kg}{m^3}]$	1510	971
Dynamic Viscosity $[Pa * s]$	1000	/
Specific Heat $[\frac{kJ}{kgK}]$	/	1.719

Remaining material data is obtained by referencing the (T, C_p) graph provided by Liang et al. [11] shown in figure 2.3. To adapt the curve to the Enthalpy-Porosity method it is necessary to obtain PCM8's latent heat in $\frac{kJ}{kg}$.

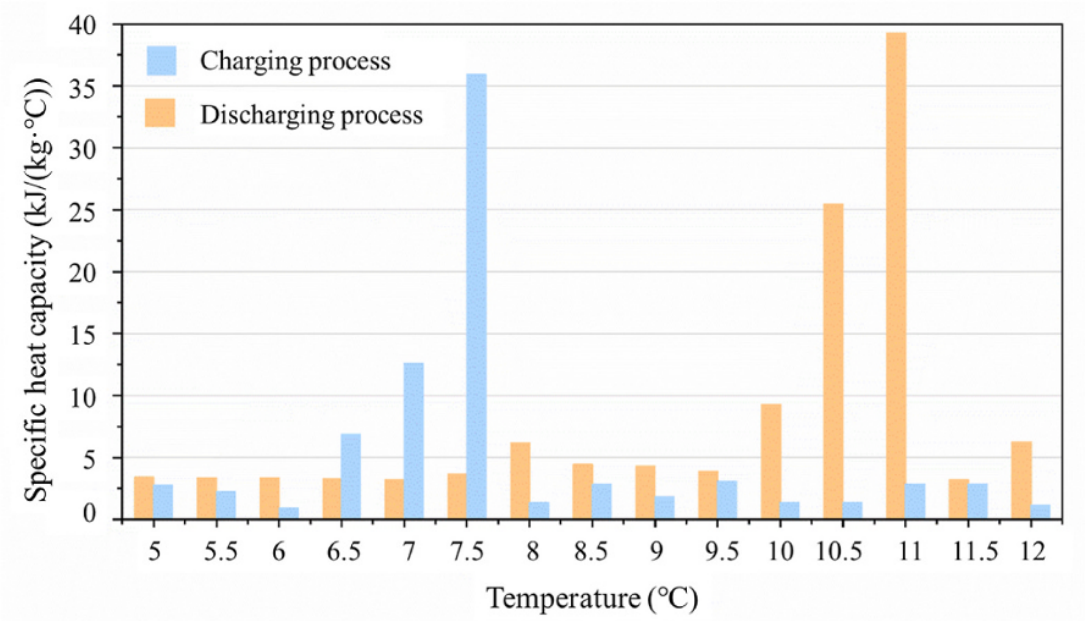

Figure 2.3: (T, C_p) graph for PCM8 for both charging and discharging phase. Source: Liang et al. [11].

After digitalizing the provided graph, an average value for C_p is obtained by considering data points outside of the declared melting range as a first approximation. This takes into account both the liquid and solid phase specific heat. Declared melting range is between 7.5 °C and 11 °C.

The integral of $C_p(T)dT$ from $T_0 = 5.5$ °C to $T_1 = 12$ °C expresses **heat absorbed by the PCM** including melting latent heat. Integration ends are chosen as the lower and upper bounds of possible temperatures for the PCM. The heat calculated is used as an abstraction to estimate latent heat.

$$q_{T_0 \hookrightarrow T_1} = \int_{T_0}^{T_1} C_p(T)dT + L \tag{2.1}$$

The provided graph, when integrated from T_0 to T_1, returns exactly $q_{T_0 \hookrightarrow T_1}$. By rearranging and using a constant $C_{p,avg}$ to simplify the sensible heat contribution:

$$L = q_{T_0 \hookrightarrow T_1} - C_{p,avg} \int_{T_0}^{T_1} dT \tag{2.2}$$

Latent heat is thus numerically obtained across the dataset as:

$$\begin{cases} L_i = (C_{p,i} - C_{p,avg})(T_i - T_{i-1}) \\ L = \sum_i L_i \end{cases} \tag{2.3}$$

where i is the index associated to each entry and the term $(T_i - T_{i-1})$ is constantly equal to 0.5 K.

Specific heat is obtained by firstly considering points outside of the melting range for the calculation of $C_{p,avg}$ and secondly by only including points below the melting range for $C_{p,sol}$ while keeping the liquid phase $C_{p,liq}$ as a different value althogether. The advantage of the first method is the ease of implementation given that a single constant C_p value is used for the simulation while the second method requires the implementation of an user defined function to blend $C_{p,sol}$ and $C_{p,liq}$ in the melting range as shown in 2.4. Both approaches are studied and compared.

Data obtained for simulation is shown in the following table along with geometry data:

	$C_{p,const}$	$C_{p,var}$
Latent heat $[\frac{kJ}{kg}]$	33.9	35.5
$C_{p,sol}$ $[\frac{kJ}{kgK}]$	3.6	3.2
$C_{p,liq}$ $[\frac{kJ}{kgK}]$	3.6	6.25

Plate dimensions [mm]	230x170x25
Plate thickness [mm]	1.8
Elementary channel length [mm]	1050
Elementary channel height [mm]	90
Horizontal plate spacing [mm]	25
Vertical plate spacing [mm]	20

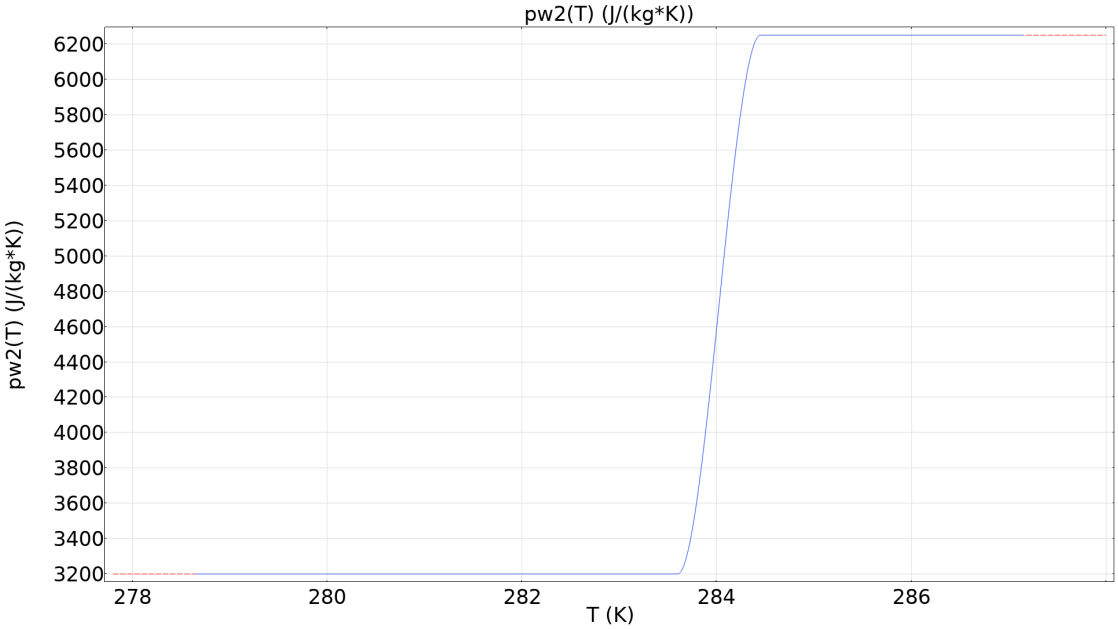

Figure 2.4: Variable C_p implementation in COMSOL.

2.2 Numerical Model and Governing Equations

In this work a 2D model is developed in order to capture a significant part of the physics involved while maintaining a favorable computation time. This characteristic makes the model well suited for repeated parametric studies and optimization tasks. Furthermore, high-level abstraction for 0D network models is another favorable prospect. While the latter is beyond the scope of this work, it is a promising application for future expansion in the current landscape for energy management and simulation [3]. Given the non-staggered geometry of the system, two symmetry axes are exploited to reduce the computational domain. One axis crosses over the middle of PCM plates where water flow field is symmetrical across two elementary channels while another symmetry axis crosses the middle of the water flow field in one elementary channel which is, again, symmetrical by nature. This is shown clearly in 2.5.

The development of a more complex 3D model may be appropriate for further research as at the time of writing literature lacks any combination of the Enthalpy-Porosity method applied to the study of thermal solutions for data centers.

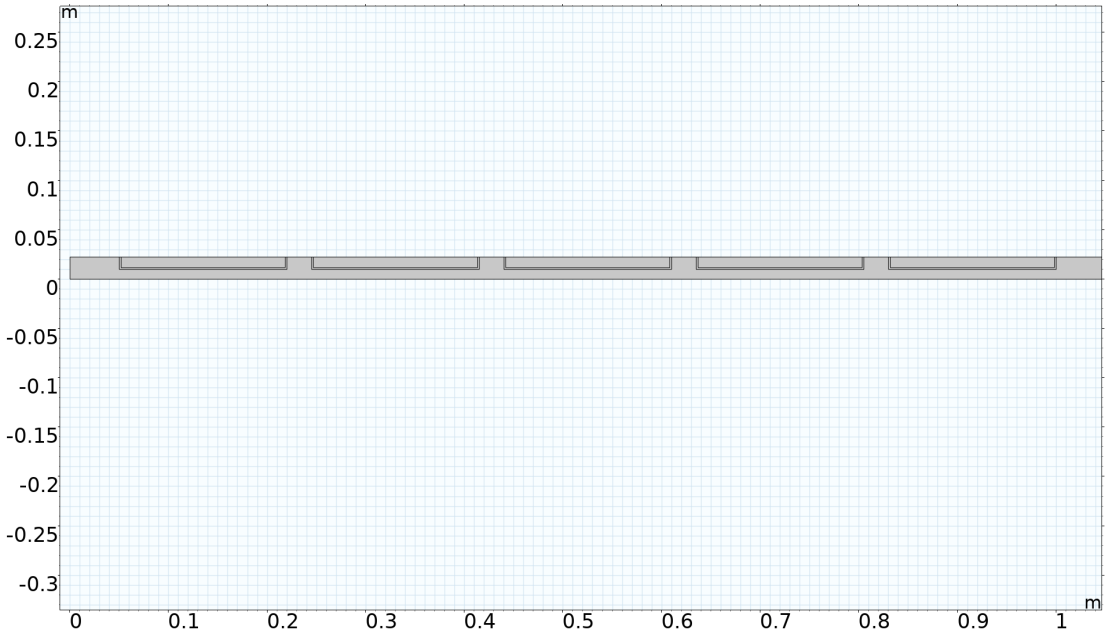

Figure 2.5: Reduced Computational Domain in COMSOL.

2.2.1 Hypotheses

The model is implemented in COMSOL by using the conjugate Heat and Mass Transfer Module with the addition of user-defined functions and source terms for the implementation of the Enthalpy-Porosity method, utilized to model the behaviour of PCM. Governing equations are solved via the Finite Element Method.

Hypotheses are as follows:

1. Density is considered constant for each subdomain (Water, HDPE, PCM).
2. Material properties are considered isotropic.
3. Viscous heating is neglected.
4. Interfacial thermal resistances are neglected.
5. Natural convection in the molten PCM field is neglected. This is a relatively strong approximation given that in the case of medium sized structures natural convection is considered a dominant heat transfer mechanism. In the present work, computational efficiency was prioritized to facilitate design-space exploration. Melting rate is expected to be slightly underestimated but in the context of a simplified preliminary exploration the tradeoff between computational time and accuracy is deemed acceptable.

6. Heat exchange towards the outside of the device is neglected.

7. Only one representative channel is considered. For all mass conservation calculations 5 total channels were considered. The hypothesis is justified by the fact that if the device is well engineered edge effects are neglectable. This is compatible with the reference setup as a perforated homogenization plate is used.

8. Water flow field is considered hydraulically developed and thus in steady state.

9. Thermal properties are considered constant except for C_p in the PCM field where applicable.

10. Gravity effects are neglected.

2.2.2 Governing Equations

Governing equations for the model are the Navier-Stokes Equations in transient form for mass, momentum and energy conservation with added source terms:

$$\nabla \cdot \mathbf{u} = 0 \tag{2.4}$$

$$\frac{\partial(\rho \mathbf{u})}{\partial t} + \nabla \cdot (\rho \mathbf{u} \otimes \mathbf{u}) = -\nabla P + \mu \nabla^2 \mathbf{u} + \mathbf{F} - \mathbf{S} \tag{2.5}$$

$$\frac{\partial(\rho C_p T)}{\partial t} + \nabla \cdot (\rho C_p T \mathbf{u}) = \nabla \cdot (k \nabla T) - S_h \tag{2.6}$$

Where $\mathbf{u}$ is the velocity field, T is the temperature field, ρ is the density, P is the pressure, k is the Thermal Conductivity, $\mathbf{F}$ is the body force, S_h is the latent heat source term, $\mathbf{S}$ is the mushy zone momentum sink term, C_p is the specific heat and μ is the dynamic viscosity . Parameters in bold are vectors.

2.2.3 Enthalpy-Porosity Method

The Enthalpy-Porosity method is from a class of methods **used for the solution of numerical problems involving phase change**. It consists in the **addition of source terms to the momentum and energy equations to model the release/absorption of heat and the implicit melting front**, treating zones undergoing phase change as porous media [21].
Phase change problems exhibit a high degree of nonlinearity due to a moving front that separates phases, generally with highly varying thermal properties. Additional challenges are posed by the modeling of bulk flows due to the moving front [21].

The Enthalpy-Porosity method is chosen as it does not explicitly track the melting front but rather **uses a function of temperature to abstract the liquid fraction** in any point of the PCM domain.
This substantially reduces computational complexity while retaining the information required to evaluate phase-change performance. Another strength of the method is the possibility of studying convective motion in phase change materials through the interaction between the momentum source terms and convective motion modelling techniques (for example, the Boussinesq approximation). Additionally, the Enthalpy-Porosity method has been widely used and validated in literature showing good accuracy and consistently fast convergence [21].

One of the pillars of the method is the definition of latent heat as following:

$$\Delta H = \phi(T) \cdot L \tag{2.7}$$

Where $\phi(T)$ is the **Liquid Fraction (LF)**. It is expressed as a function of temperature field in each point of the PCM domain as:

$$\phi(T) = \begin{cases} 0 & \text{if } T < T_m - \frac{\Delta T}{2} \\ \frac{T-(T_m-\frac{\Delta T}{2})}{\Delta T} & \text{if } T_m - \frac{\Delta T}{2} \leq T \leq T_m + \frac{\Delta T}{2} \\ 1 & \text{if } T > T_m + \frac{\Delta T}{2} \end{cases} \tag{2.8}$$

This adimensional parameter quantifies how molten the material is relation to its temperature. Through this quantity it is possible to implicitly track the "melting front".

In this work a value of $\Delta T = 5\ K$ was chosen. While not strictly adherent to PCM8's melting range the choice of this melting range favors numerical convergence and consistency. This is relatively common in literature, one example is the work from Agegnehu et al. [29] who clearly state that the choice of $\Delta T = 5\ K$ while not completely accurate is a great compromise between accuracy and convergence.

The **Darcy Source Term Method (Darcy STM)** is used to model the kinematic behaviour in the mushy zone where the PCM is neither completely solid or liquid. It consists in the addition of a source term in the momentum equation to force a null speed state when PCM is solid and to modulate the velocity field in the mushy zone up to the completely "free" molten velocity field.

$$S = C \left(\frac{(1-\phi(T))^2}{\phi(T)^3 + \varepsilon} \right) \tag{2.9}$$

where C is the mushy zone constant and ε is a small constant needed to avoid zero division. Their values are set to $C = 5 \cdot 10^5\ \frac{kg}{m^3 \cdot s}$ and $\varepsilon = 0.001$.

For the energy equation, the **latent heat source term** is added and computed as:

$$S_h = \frac{\partial(\rho \Delta H)}{\partial t} + \nabla \cdot (\rho \Delta H \mathbf{u}) \tag{2.10}$$

This source term expresses the absorption / release of heat through the variation of ΔH in time and the advection of latent heat energy through the second term.

2.2.4 PCM8 model specifications

PCM domain is set to be a fluid in laminar flow regime. The Darcy source term in the momentum equation regulates the flow field from null in solid regions to free circulation in liquid regions with a transition mushy zone regulated by the C coefficient.

Depending on the chosen method for the calculation of latent heat, specific heat is either considered constant or a function of temperature. For the latter option an user defined piecewise function is implemented in COMSOL around T = 11.5 °C. To avoid convergence issues due to steep variations in thermal properties, the function is smoothed at the ends as previously shown in 2.4.
For the flow field, no-slip condition is applied at the wall (1, 2, 3) while symmetry condition is applied at the upper bound (4) in reference to figure 2.6. Equations are solved in transient state. Since natural convection is neglected, the motion field is initialized to 0 and inertial terms are excluded. This solution improves numerical stability while ensuring a constantly null flow field across all PCM plates barring some numerical diffusion.

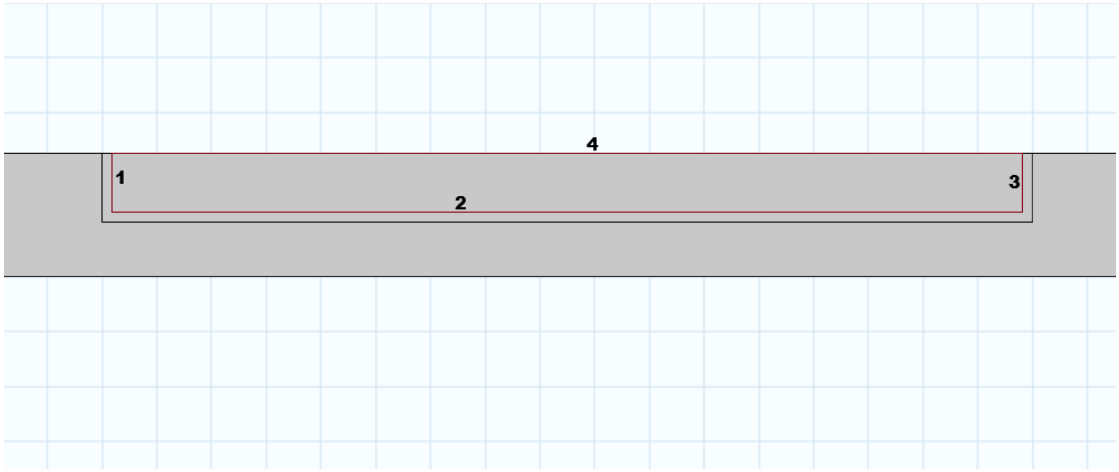

Figure 2.6: PCM Domain Boundary Condition Scheme.

$$\mathbf{u}\Big|_1 = \mathbf{u}\Big|_2 = \mathbf{u}\Big|_3 = 0 \tag{2.11}$$

$$\left.\frac{\partial \mathbf{u}}{\partial \mathbf{n}}\right|_4 = 0 \tag{2.12}$$

For the energy equation, symmetry condition is applied at the upper boundary (4). Other boundaries are considered internal in respect to the solution of the energy equation in the model so they are automatically set to heat flux continuity by the software.
Given the hypotheses on PCM's flow field the advective term in the energy equation source term is neglected, significantly improving computation time and stability.

$$\left.\frac{\partial T}{\partial \mathbf{n}}\right|_4 = 0 \tag{2.13}$$

PCM8 is initialized to its charged state so the initial condition for Temperature is $T_{in} = 5.5$ °C.

The same structure is repeated for each PCM plate.

2.2.5 Water model specifications

Water flow field is obtained in its stationary form. This is derived from the reasonable hypothesis that flow transient is negligible compared to the thermal timescale. Flow field is solved by neglecting the inertial terms: formally creeping flow happens at $Re << 1$ but the assumption is made to simplify the model without extreme loss of accuracy. The hypothesis is also supported by Liang et al. [11] who show a simulated flow field that is clearly symmetrical. Flow field is shown in 2.2. Boundary conditions are set so that at the interface between HDPE plating and water no-slip condition is applied (HDPE Walls). A constant normal velocity profile is set for the inlet (in) and for the outlet a constant pressure condition is applied (out). Furthermore, back propagation of pressure waves is mitigated by applying a homogeneous Neumann condition to pressure on the outlet. In the lower part of the simulation domain where the symmetry axis lies, symmetry condition is applied (sym).

$$\mathbf{u}\Big|_{HDPE\ walls} = 0 \tag{2.14}$$

$$\left.\frac{\partial \mathbf{u}}{\partial \mathbf{n}}\right|_{in} = 0.012\ \frac{m}{s} \tag{2.15}$$

$$P\Big|_{out} = P_{out} \tag{2.16}$$

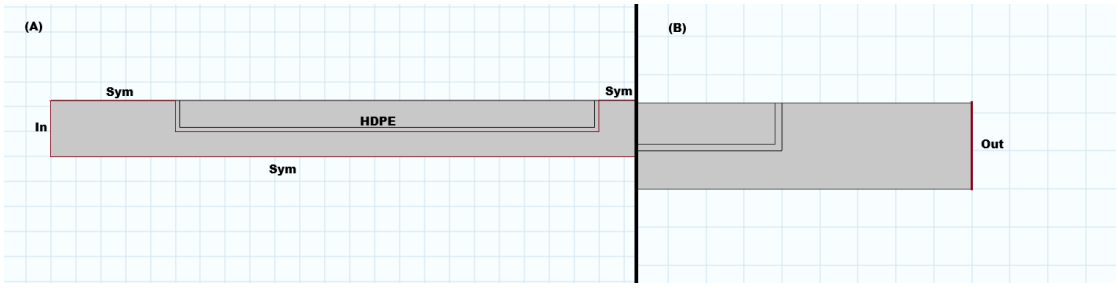

Figure 2.7: Water domain boundary conditions scheme. (A) is the inlet portion of the system, (B) is the outlet portion. Water flow moves left to right.

$$\left.\frac{\partial \mathbf{u}}{\partial \mathbf{n}}\right|_{sym} = 0 \tag{2.17}$$

For the energy equation, symmetry condition on water temperature flow field is applied along both symmetry axes (sym). For the inlet, a constant Dirichlet condition is applied to simulate the intake of hot water for the discharging process at $T_{in} = 12$ °C (in). Homogeneous Neumann condition is applied to the outlet to avoid back propagation of thermal waves (out).

$$T\Big|_{in} = T_{in} \tag{2.18}$$

$$\left.\frac{\partial T}{\partial \mathbf{n}}\right|_{sym} = 0 \tag{2.19}$$

$$\left.\frac{\partial T}{\partial \mathbf{n}}\right|_{out} = 0 \tag{2.20}$$

Initial condition for the temperature field is set to $T_{in} = 5.5$ °C as this simulates a fully charged device.

2.2.6 HDPE model specifications

The only equation that applies to the HDPE domains is the energy equation. The only applicable boundary conditions are the ones on the upper symmetry axis (sym). The remaining boundaries are internal thus heat flux continuity is applied automatically as no contact thermal resistence is modelled.

$$\left.\frac{\partial \mathbf{T}}{\partial \mathbf{n}}\right|_{sym} = 0 \tag{2.21}$$

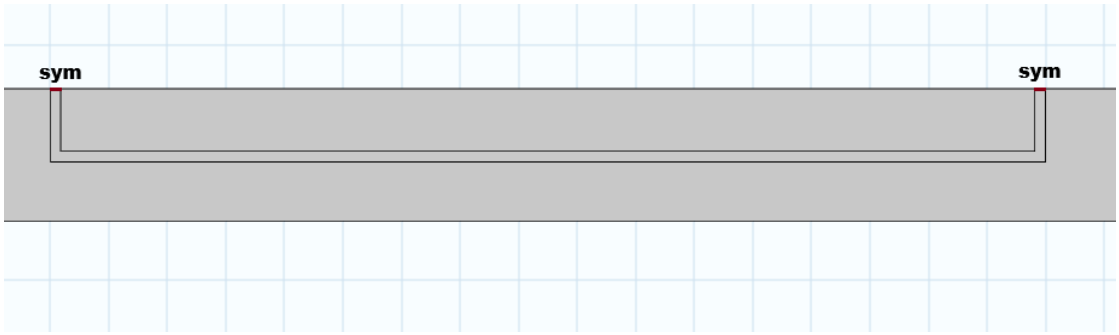

Figure 2.8: HDPE Domain Boundary Conditions Scheme.

2.3 Results

Simulations are run in COMSOL ver. 6.3 with automatically scaled time stepping with a minimum timestep of 500 s. Simulation time is 30.000 s in order to closely match experimental results.
Experimental curves are obtained graphically from the work by Liang et al. by sampling every 1250 s. Graphical uncertainty is estimated to be ±0.1 °C. Furthermore, Liang et al. report an uncertainty of plus or minus 1.2 °C due to the thermocouples used [11].
Reference experimental curves relate to measurements in the middle of the bulk of each plate and, in particular, they are from three adjacent plates in one singular elementary channel. The curves provided relate to the discharging phase (PCM Melting) which is the one simulated.

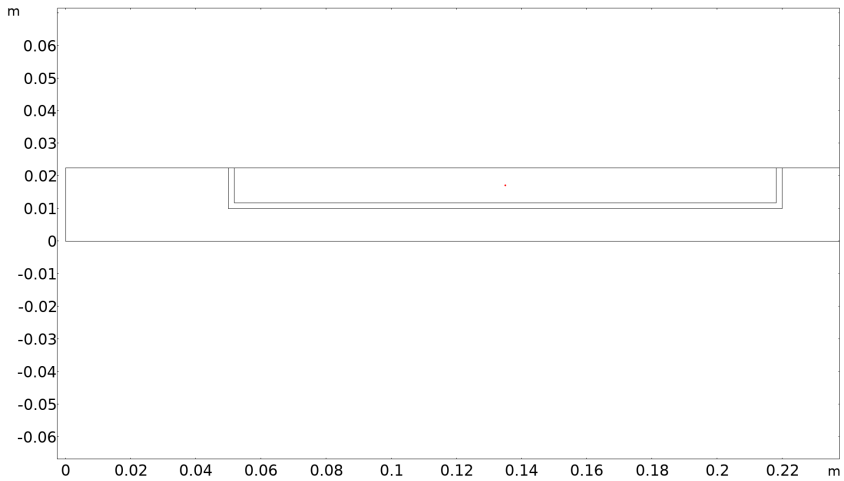

Figure 2.9: T1 point sensor placement in COMSOL.

Three point probes are placed in the middle of each PCM8 domain in COMSOL as demonstrated in image 2.9. They are used to obtain the time evolution curves of temperature (and by extension, liquid fraction) in the bulk point. A comparison of the experimental dataset and the simulated points is plotted by interpolating in 1.250 s increments through COMSOL and by using Matlab to plot the results.

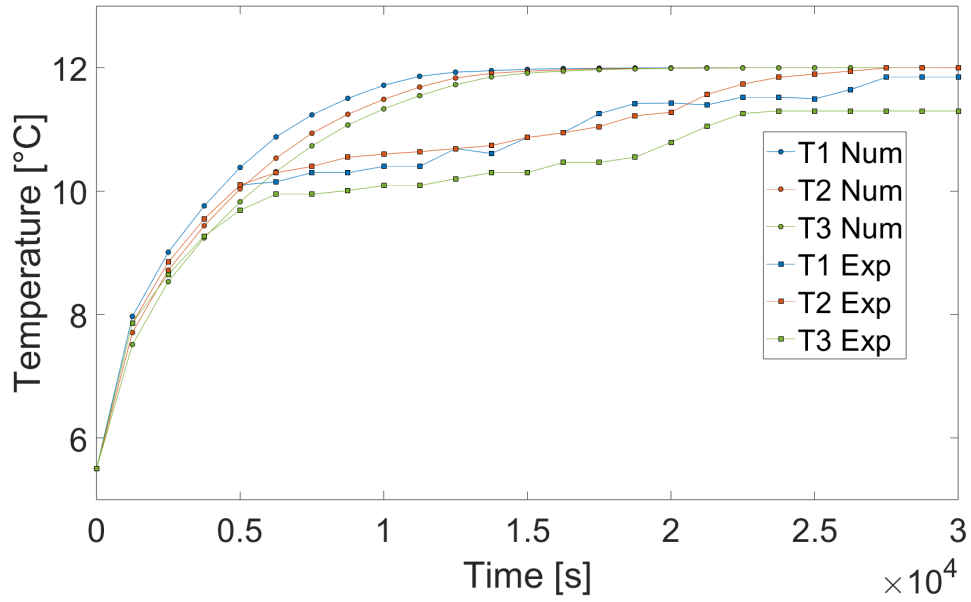

Figure 2.10: Plot of temperature profiles. "Num" curves refer to numerical results while "Exp" curves refer to experimental results from the reference work.

Results are shown for the case in which C_p is implemented as a piecewise temperature function.
To validate the accuracy of the model the metrics used are e_{rel}, MSE, RMSE and RMSEP and they are evaluated as follows:

$$e_{rel,i} = \frac{T_{exp,i} - T_{num,i}}{T_{exp,i}} \tag{2.22}$$

$$MSE = \frac{1}{N}\sum_i (T_{exp,i} - T_{num,i})^2 \tag{2.23}$$

$$RMSE = \sqrt{MSE} \tag{2.24}$$

$$MSEP = \frac{1}{N}\sum_i e_{rel,i}^2 \tag{2.25}$$

$$RMSEP = \sqrt{MSEP} \tag{2.26}$$

The following table contains the metrics that inform the validation of the model:

	T1	T2	T3
RMSE ($C_{p,var}$)	0.79	0.64	1.03
RMSEP ($C_{p,var}$)	7.4 %	5.9 %	9.9 %
RMSE ($C_{p,const}$)	0.85	0.71	1.10
RMSEP ($C_{p,const}$)	8.0 %	6.6 %	10.6 %

Additional Comments

As can be observed, **the model shows good agreement with the experimental data during the initial discharge transient and throughout the phase-change temperature plateau**. The latter is associated with latent heat absorption and, although clearly visible, remains relatively limited due to the modest latent heat capacity of PCM8.
Late fusion remains relatively critical: the model shows thermal overshoot as the PCM bulk reaches water temperature at t=6.250 s rather than staying between 9.5 °C and 11 °C for the central part of the process (between 5.000 s and 20.000 s) as seen in the experimental curves. This is possibly due to the skew of surface to volume ratio which is not captured well by a 2D model or non-ideal interfacial contact which is neglected in this study. The model reaches quiescence temperature at $t = 15.000\ s$ while experimental data shows that the device reaches the same equilibrium at around $t = 22.500\ s$. The best agreement with experimental data is seen with T1 and T2 sensors while the T3 sensor shows the most discrepancy. Regardless, the maximum absolute error is still comparable with the declared thermocouple reading inaccuracy reported by Liang et al.
Overall, the current results can be considered satisfactory for the intended application. Although the two-dimensional formulation does not capture all relevant physical phenomena with the same fidelity as a full three-dimensional model, it provides a favorable compromise between accuracy and computational cost. This balance makes the proposed framework particularly suitable for computationally intensive tasks such as topology optimization, design-space exploration, and extensive parametric studies.

Mesh Convergence Analysis

A mesh independence analysis is run by considering 3 different factors across various mesh sizes. Standard COMSOL meshing is used for the analysis with standard mesh sizes being "Coarser", "Coarse, "Normal", "Fine" and "Finer". For each a table reports the number of elements. A physics adaptive mesh was used to better capture the steepest thermal gradients at the interfaces. The model used for the

analysis is the $C_{p,var}$ version which is the one effectively used throughout the rest of the work.

	Mesh Elements
Finer	92965
Fine	52838
Normal	33761
Coarse	17800
Coarser	11025

Parameters considered are:

1. Average water outlet temperature.
2. T1 temperature profile.
3. Heat exchanged at the PCM boundaries.

The average water outlet temperature does not see a particular difference between the mesh sizes except for the initial transient where the "Finer" mesh differs in 3.5% in respect to the "Fine" mesh. For the remainder of the simulation a relative difference of less than 1% can be seen which is deemed acceptable.
T1 shows a similar trend, the initial transient is where most of the difference between the meshes lies. "Coarse" and "Normal" meshes differ up to 2.54% while "Finer" and "Fine" show a difference that is markedly less than 1% with all meshes converging to the same result.
Heat exchanged from PCM shows the most difference with all classes below "Fine" showing very similar results. The jump from "Finer" to "Fine" shows that the models closes with a relative difference of 3.66% on total energy exchanged at the boundary while other meshes constantly stay under 1.1% relative difference between them.

Results justify the use of the "Fine" mesh for this work since metrics used for KPIs and validation do not change much between "Fine" and "Finer" and a 3.66% difference in energy exchanged at the PCM boundary is acceptable. The choice is made to favor computational costs for later parametric sweeps. Furthermore, values obtained are in line with what is declared by Liang et al. in their appendix where they declare a difference of 3.6% on the temperature field between the used grid and the higher order one.

Comparative Analysis

Liang et al. use the indicated device as a testing platform to succesfully design an upscaled version of a retro-fit for a Data Center with a consumption of 8084

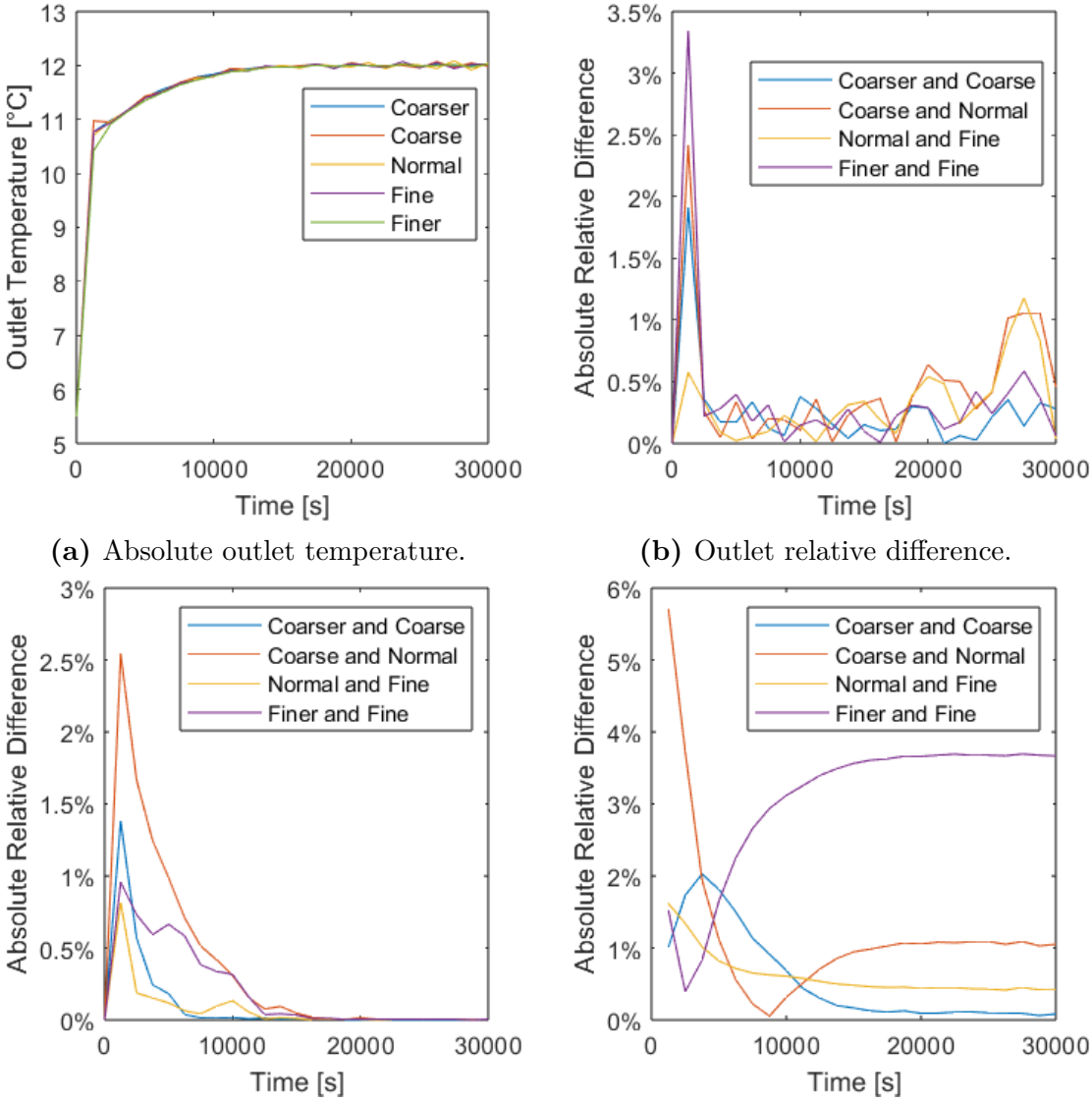

(a) Absolute outlet temperature.

(b) Outlet relative difference.

(c) T1 relative difference.

(d) Heat from PCM relative difference.

Figure 2.11: Mesh convergence study parameter plots.

kW. For the up-scaling a different packing geometry and boundary conditions are employed thus raising energy density and energy distribution. They indicate that a traditional water tank only contains 26.67% of the energy included in the PCM based cold energy storage tank for their new conditions with equal size. This shows that their optimized device, obtained from RSM applied to the testing device, can succesfully be up-scaled to real case scenarios. For the testing device however the ratio is not as favorable. From 5.5 °C to 12 °C the device is able to store 1809 kJ

of thermal energy. The testing device compared to a traditional water tank (with volume equal to the device going from perforated plate to perforated plate) does not offer higher energy density as it stores 35% less total energy. The device, while energetically not as packed as a traditional water tank, is capable of keeping water outlet temperature under 12 °C for up to 2.38 h according to simulations. While results show an evident ability to manage water temperature under emergency conditions, **by replacing PCM8 with a more energy dense PCM it is possible to store 18.6% more energy compared to an equivalent water tank**. This is done by employing RT10HC, a PCM by RubyTherm, which will be examined in the following chapter. This solution combines the modest geometrical packing of the control device with a highly energy dense PCM solution.

Volume $[m^3]$	0.089
Water tank energy [kJ]	2437
PCM based cold energy storage device energy (PCM8) [kJ]	1809
PCM based cold energy storage device energy (RT10HC) [kJ]	2995

Chapter 3

Design Optimization

The device proposed by Liang et al. is a compact heat exchanger that works as a thermal battery. PCM is encapsulated in relatively narrow rectangular plates ensuring a decent area for heat exchange. As mentioned in the introduction, tone of the main limitations of PCM-based thermal batteries is the **inherently low thermal conductivity of most PCMs**. In this device the plating material, HDPE, has a similar conductivity to that of PCM. This means that most design optimization methods explored in the preliminary review are not adequate as they are based on the usage of higher conductivity plating material. Because of this, the introduction of additional HDPE structures within the PCM domain provides only limited enhancement of conductive heat transfer pathways. Topological Optimization and internal HDPE finning would technically work, as demonstrated by Liang et al. [11], but in this work the idea of **adding independent hotspots** in the bulk is proposed. Independent hotspots are internal heat exchange pathways that are hydraulically independent from the water entering the device in the normal configuration. This arrangement generates new hotspots in the most critical parts of the PCM domain while ensuring the same entrance temperature for each subchannel thanks to the hydraulic segregation. Compared to the solution by Liang et al. [11] this arrangement ensures **more consistent heat pathways** by means of enforcing a stronger temperature gradient rather than generating new heat travel paths with low conductivity material (HDPE).
To implement the proposed solution **additional cross-flow channels** are introduced perpendicular to the two-dimensional computational plane. In the physical device, these channels extend through the third dimension and allow water to exchange heat directly with the PCM through cylindrical HDPE walls. Keeping the HDPE material choice ensures the device can still operate with plastic plating, reducing manufacturing costs compared with metallic solutions and corrosion resistance against salt hydrates and liquid metal PCMs [11] [17]. Paraffins on the other hand do not exhibit this issue as they are not corrosive for metal but the

employment of HDPE extends the range of usable PCMs which is deemed critical for scalability to different classes of operation.

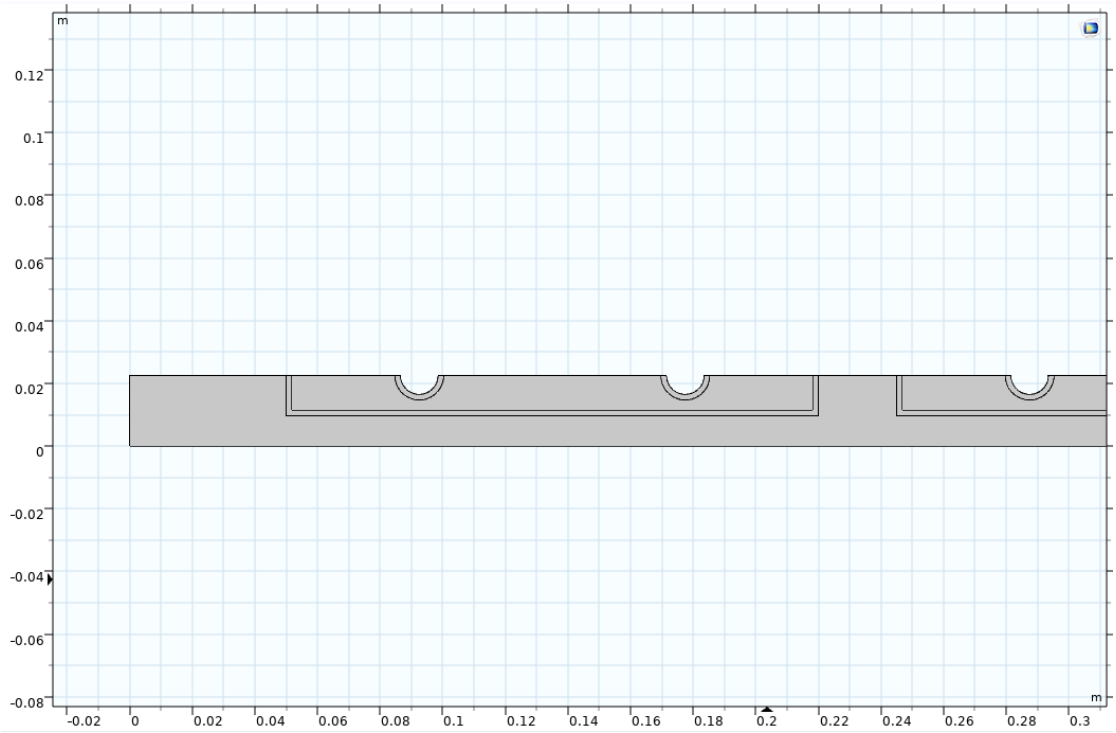

Figure 3.1: Proposed geometry in COMSOL with $D_p = 12\ mm$ and hole spacing equal to 0.085 mm.

For the optimization a new PCM by RubyTherm is employed. The model used is the RT10HC, chosen for its high heat storage capacity and for its melting point, adequate in respect to the boundary conditions of the problem. Material properties were obtained from the manufacturer's technical datasheet [30].

A (C_p, T) graph is provided in the same form of the one provided by Liang et al. in their work so the same methodology is used to obtain data for simulations. Calculations are done considering only the part of the graph that includes the working temperatures of the simulation to ensure the usage of relevant data.
The numerical model used for simulations employs a variable C_p user defined function with the same smoothing parameters used for the validation model.
A phase-change interval of $\Delta T = 3$ K was adopted to reflect the narrower melting range of RT10HC while preserving numerical stability.

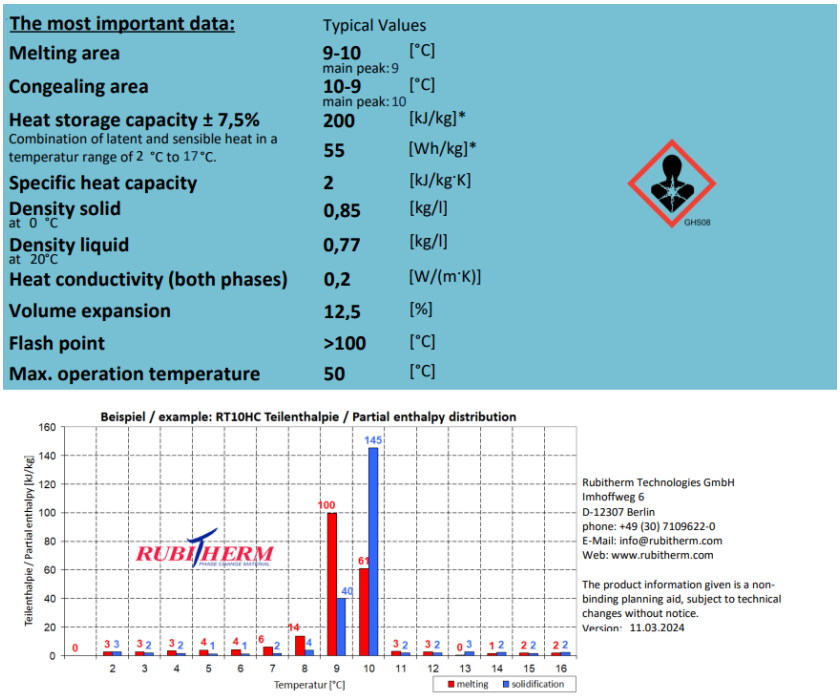

Figure 3.2: RT10HC Data Sheet.

3.1 Benchmark device

The benchmark device used for comparisons (Case 0) is geometrically identical to the one proposed by Liang et al. with the difference that the simulation employs material data that represents RT10HC. A table is provided with all simulation data obtained from the spec sheet. Where not specified, simulation parameters are identical to the validation case. Contrary to PCM8, density is provided for both liquid and solid phase but for simulation an average value between the two is used.

Latent Heat $[\frac{kJ}{kg}]$	157
$C_{p,sol}$ $[\frac{kJ}{kgK}]$	3.8
$C_{p,liq}$ $[\frac{kJ}{kgK}]$	2.77
ρ_{avg} $[\frac{kg}{m^3}]$	810
Thermal Conductivity $[\frac{W}{mK}]$	0.2

3.1.1 Key Performance Indicators (KPIs)

To study performance across different configurations some KPIs are defined to track common metrics. They are defined on the basis of **integral averages** on the PCM domain for two reasons:

1. Tracking overall performance on a plate-to-plate basis.

2. Independence from local hotspots and local numerical oscillations at interfaces.

Because the proposed optimization introduces localized heat exchange channels, pointwise temperature measurements become highly sensitive to local thermal gradients and mesh-dependent effects. Domain-averaged quantities are therefore preferred to characterize the global thermal response of each PCM plate. Furthermore, discharging performance may be overestimated by only examining pointwise measurements due to their placement in close proximity of the highest temperature gradients. In addition, in some configurations the geometrical placement of sensors is out of domain due to the new geometry making the point probe approach used for validation an unsuitable mean of recording data. Quantities of interest are **average liquid fraction**, **average plate temperature** and **average water outlet temperature** and they are respectively defined as follows:

$$\langle \phi \rangle(t) = \frac{1}{\Gamma_{PCM}} \int_{\Gamma_{PCM}} \phi(T)\ d\Gamma \quad , \quad T = T(\mathbf{x}, t) \tag{3.1}$$

$$\langle T_{PCM} \rangle = \frac{1}{\Gamma_{PCM}} \int_{\Gamma_{PCM}} T\ d\Gamma \quad , \quad T = T(\mathbf{x}, t) \tag{3.2}$$

$$\langle T_{out} \rangle = \frac{1}{L_{out}} \int_{L_{out}} T\ dl \quad , \quad T = T(\mathbf{x}, t) \tag{3.3}$$

Average liquid fraction is used as an auxiliary parameter to define two characteristic melting times: τ_{80} and τ_{95}. They are defined as the time in which the most disadvantaged plate (last one with respect to main water flow, plate 5) reaches, respectively, 80% and 95% average liquid fraction. Those parameters are used for the calculation of average power and they express how the system behaves dynamically. The 80% threshold captures the high-power portion of the discharge process, whereas the 95% threshold characterizes the final stages of melting, where the reduction of thermal gradients progressively limits heat transfer rates. The two KPIs are thus valid to study both initial and late discharge processes. These indicators do not directly characterize the thermal response of the working fluid.

Therefore, they are complemented by the outlet water temperature, which provides additional information regarding heat exchanger effectiveness and thermal power delivery.

3.1.2 Benchmark Results

Simulations exhibit a qualitatively equal behaviour to that of the PCM8 version.

average temperature profiles show that, similarly to the PCM8 version, there is a steep temperature change due to pre-fusion heating where PCM behaves as a simple solid. As soon as the average temperatures reaches the melting range a very visible plateau can be seen. This is much more prominent given that RT10HC exhibits much higher latent heat compared to PCM8. Once the plate is very close to fully liquid curves exhibit a different slope based on the liquid phase C_p. Interestingly, even if the liquid phase C_p is lower compared to the solid phase, the curve slope is less steep and thus the post-melting temperature rise occurs more slowly. This behavior is not governed by the thermal capacity of the PCM but rather by the decreasing temperature difference between water and PCM at that point of the discharge process. This results in a much slower rate of energy exchange. As the discharge process advances, the reduction in thermal driving force leads to lower heat transfer rates and thus explains the slower temperature increase. Furthermore, the behaviour observed is well described by τ_{80} and τ_{95}.

Average liquid fraction has a more regular trend. The integration absorbs local gradients where PCM melts faster and colder spots where PCM melts slower thus regularizing the trend on the domain-level and showing the overall performance of the device. Curves show decreasing steepness as the simulation progresses due to the increasingly slower rate of energy exchange as mentioned before.
τ_{80} and τ_{95} are respectively 17.900 s and 24.200 s.

Average water outlet temperature is very much influenced by velocity. For this problem the kinematic scale is much smaller than the thermal one and thus convective heat transfer is the dominant phenomenon as will be explored more thoroughly later. The curve has an extremely steep initial climb where hot water quickly fills the device and then, thanks to heat exchange with PCM plates, it flattens and the thermal management effect is achieved. After the initial transient the curve stops around control temperature and climbs with a quasi-linear behaviour to steady state equilibrium at 12 °C.

Energy balance is well posed. It is possible to calculate the thermal energy stored in PCM from 5.5 °C to 12 °C via data sheet. By calculating total PCM mass using the liquid density (this assumes injection of PCM in the plates in the

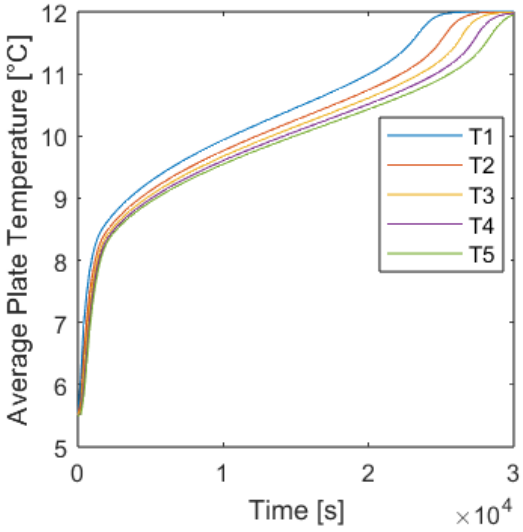

(a) PCM plates average temperature.

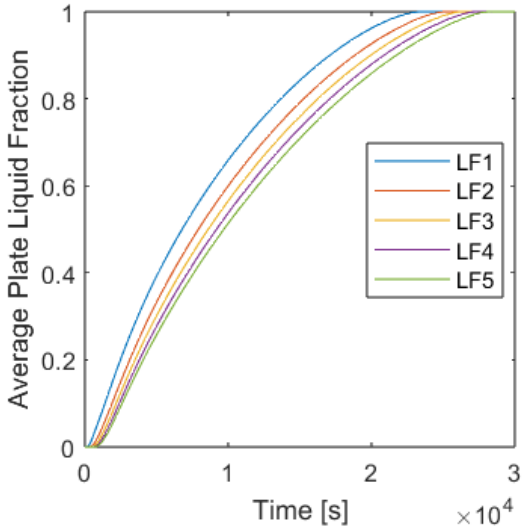

(b) PCM plates average liquid fraction.

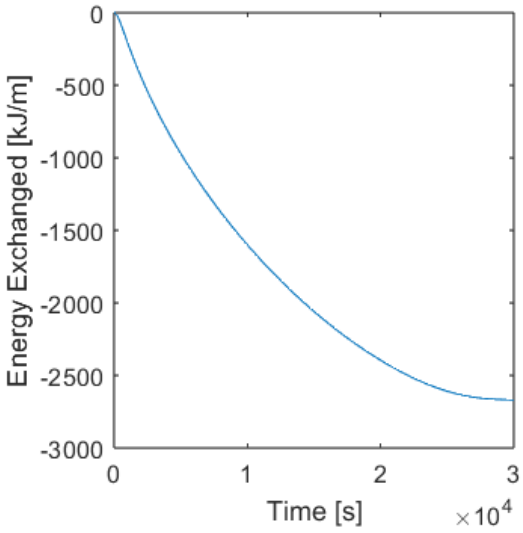

(c) Energy exchanged by water.

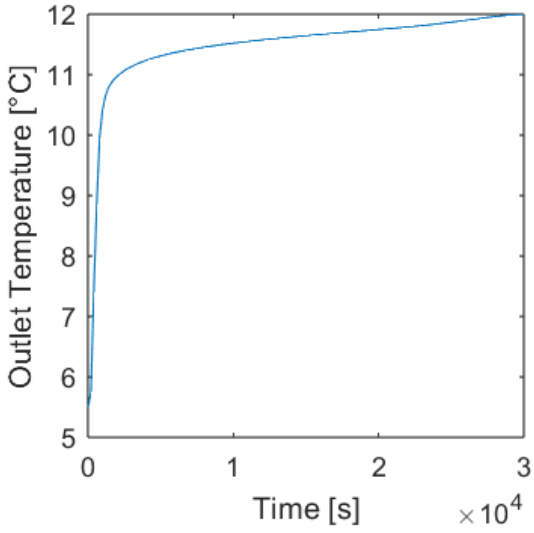

(d) Outlet temperature line average.

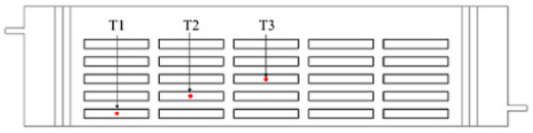

(e) PCM plate numbering system. Points are staggered but they refer to a single in-line row. Source: Liang et al. [11].

Figure 3.3: Benchmark case results.

liquid phase) the energy provided by the PCM in the whole discharging process is obtained.
From COMSOL, thanks to the cumulative operator, the total energy exchanged at the PCM boundary per unit length is obtained. It is then multiplied by the "collapsed" third dimension to obtain effective energy exchanged. By comparing theoretical and simulated energy it is possible to see that **the model shows a difference of just 0.8**% compared to the theoretical value. This value reflects how the model accurately predicts stored energy and justifies the use of cumulated energy at the boundaries as a parameter to calculate average power delivery. The approach is not meant to assess the exact quantity of energy exchanged given the approximations made on density and latent heat but rather it shows that **energy conservation** is achieved. Furthermore, RubyTherm reports a variation of plus or minus 7.5% with respect to heat capacity from 2 °C to 17 °C: this further reinforces the point made about absolute numbers against model predictability.

3.2 Optimization Process

The bottlenecks for PCM based devices, as mentioned before, are mostly due to thermal conductivity. Given the design challenge of being unable to create new thermal pathways from casing material, the idea of adding hotspots in the PCM bulk is a valid candidate. By injecting water perpendicularly to the 2D simulation plane a crossflow heat exchanger is made. This is achieved by adding secondary channels (2, 3, 5 channels) in which part of the total mass flow is directed. They are equally made from HDPE and their thickness is the same as the plating and they run through the whole width of the plates.
The usage of crossflow is not novel and has been shown to improve heat exchange when PCM is used [19]. Furthermore, this work focuses on studying how geometrical parameters that characterize the problem affect outcome and key quantities. This is shown to be a critical part of the optimization process as demonstrated by Rabiea et al. [31] who show that in a tube-in-tube heat exchanger with PCM the placement of the internal channel with respect to the PCM bulk strongly affects performance. Khedher et al. [32] on the other hand approach the problem with an idea similar to the one proposed in this work. They design a serpentine shaped heat exchanges that crosses the bulk of the PCM domain increasing heat exchange area and favoring internal circulation around the hotspots. They showed an improvement of up to 18.3% in the device's thermal storage capacity.

As such, in this work the number of channels, total mass flow, internal channel diameter and channel spacing will be candidates for multiple parameter sweeps in order to ascertain and quantify the role of each variable in order to obtain insights about pros and cons of each operational setting.

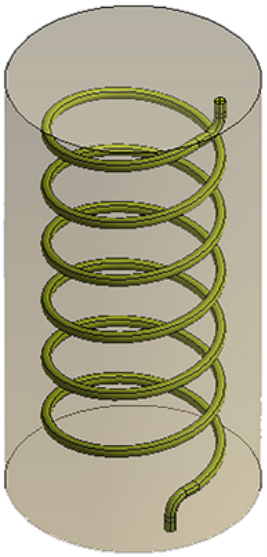

Figure 3.4: Cylindrical PCM thermal battery with internal serpentine for heat exchange. Source: Khedher et al. [32].

3.3 Model Adaptations

The model is adapted to the case in which 30% of total mass flow is directed into secondary channels. To adjust for this condition, the inlet speed is chosen so as to ensure the right flow rate.
To account for the flux in the secondary channels a simplification is needed. The 2D model can't account for the behaviour of water in the perpendicular plane. The kinematic timescale for the secondary channels is negligible in comparison the timescale of the simulation. As such, the choice made consists in enforcing a **Robin boundary condition for thermal flow at the auxiliary channels interfaces**. This is justified by the fact that the remote temperature for inlet water in the secondary channels is constant. Furthermore given the low time spent exchanging heat with the PCM it's not unreasonable to assume remote temperature for core part of the flow in the auxiliary channels. This condition, while being a simplification, **allows the model to remain conservative in terms of energy**. Robin condition is applied to the internal boundary of the perpendicular PCM tubes and it's expressed as follows:

$$q = h_c(T_{inf} - T) \tag{3.4}$$

Where h_c is the forced convection heat exchange coefficient, T_{inf} the remote temperature, q is the heat exchanged at the boundary and T is the temperature at

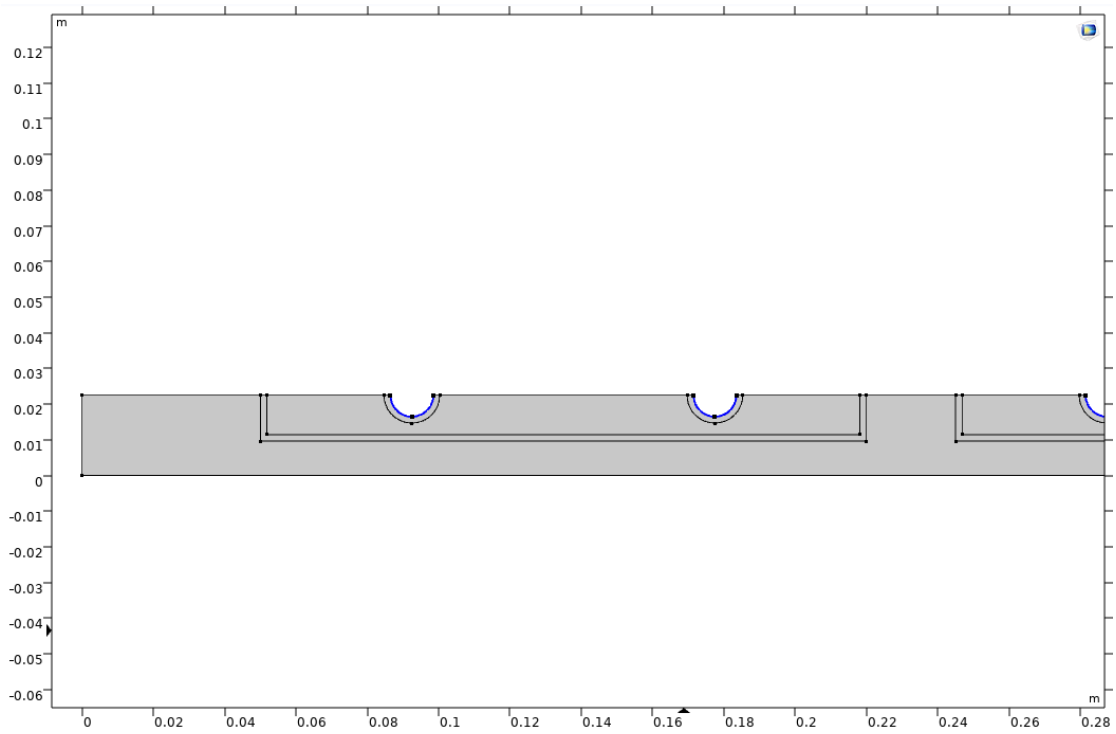

Figure 3.5: Robin boundaries as set in COMSOL.

the boundary.

The advantage of this type of boundary condition is that **the direction of energy transfer is consistent with the temperature field in the PCM domain and the projected remote temperature** which is exactly the same as the quiescence temperature for the whole system ($T_{inf} = 12$ °C). This ensures that **the simulation does not run into any extraneous heat exchanges**. Furthermore, with this condition, temperature is enforced by the energy balance at the boundary itself rather than external forcing as may be otherwise done with a Dirichlet condition. The latter is by definition not conservative and presents many modelling complications for no added benefit in this case.

To obtain the convective heat exchange coefficient some observations and hypotheses are made about the flow in secondary channels:

1. Flow is laminar in each setting.
2. Flow is hydrodynamically developed at the entrance.
3. Flow is not fully thermally developed.

4. Flow is fast enough to be able to consider internal remote temperature equal to the inlet temperature.

For this problem the Graetz number is obtained as:

$$Gz = \frac{RePrD}{L} = 6.3 \sim 15.7 \tag{3.5}$$

where Re is the Reynolds' number, Pr is the Prandtl's number, D is the channel diameter and L is the channel length.
Gz is an adimensional grouping for forced laminar flows that is used to determine whether a flow is fully developed or not in a specific channel. For values of $Gr \geq 20$ generally flow is considered developed. In this case the undeveloped thermal flow requires the usage of an appropriate correlation to obtain the forced convection heat transfer coefficient. Hausen correlation is chosen as the hypotheses required for its usage are respected except for constant wall temperature. Given that the possible temperature range for the wall is between 5.5 °C and 12 °C the approximation is deemed acceptable. The equation is used to calculate an average Nusselt number for auxiliary channels from which the convective heat transfer coefficient is obtained:

$$Nu_{avg} = 3.66 + \frac{0.668(D/L)RePr}{1 + 0.04[(D/L)RePr]^{2/3}} \tag{3.6}$$

From which:

$$Nu_{avg} = \frac{h_c D}{k} \quad ; \quad h_c = \frac{Nu_{avg} k}{D} \tag{3.7}$$

By using the Hausen correlation in conjunction with diameter parameter sweeps (which correspond to auxiliary channel flow speed to maintain mass conservation) different values for h_c are obtained and **the tradeoff between heat exchange area and forced convection coefficient is investigated**.
Furthermore, **PCM plate height is adjusted for each diameter in order to keep PCM mass constant** throughout each possible device alteration.

3.4 Results

Results are described using an alphanumeric system that consists of a letter and three numbers following the logic behind parameter sweeps. Secondary flux is kept to a constant 30% of total mass flow rate for this study. 5 flow rates are evaluated as functions of the nominal flow rate indicated by Liang et al. at 120%, 160%, 60% and 80% of nominal value. For each flow rate inlet velocity is indicated by the first number after the letter. The first letter indicates the number of auxiliary channels, the fourth number indicates which parameter is being sweeped and the third number identifies the value taken by the parameter itself. In this paragraph the term "physical water" will be used to describe fluid flow inside the simulated 2D plane while "aux water" will refer to the fictitious flow modelled by the Robin condition.

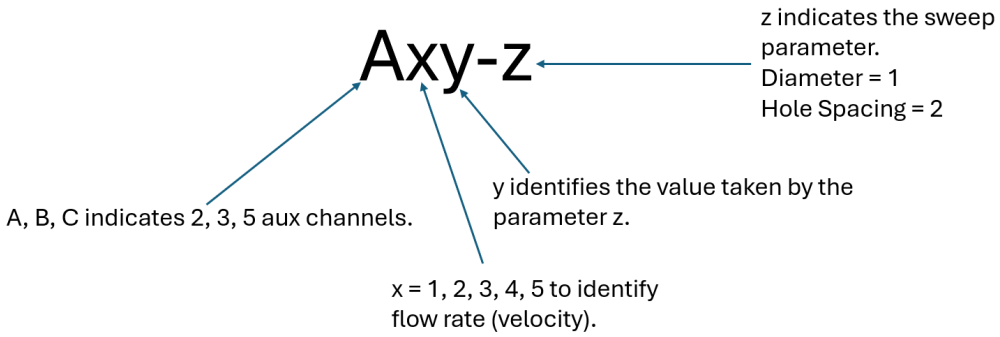

Figure 3.6: Alphanumerical system used to identify sweeps.

2 Channels - A

The first sweep consists in the addition of two hotposts to the bulk of the PCM via auxiliary channels. 8 diameters are investigated at this stage ranging from 12 mm to 5 mm. For this sweep the heightening of the plate caused by the addition of channels is minimal compared to the case with 3 and 5 channels. Because of this a wider amount of diameters is investigated to obtain clearer insights that are less affected by the striction effect. The striction effect is the acceleration of flow between two vertically aligned plates and it becomes more pronounced as plate height increases.

Graphs show average outlet temperature for simulated water inside the device.

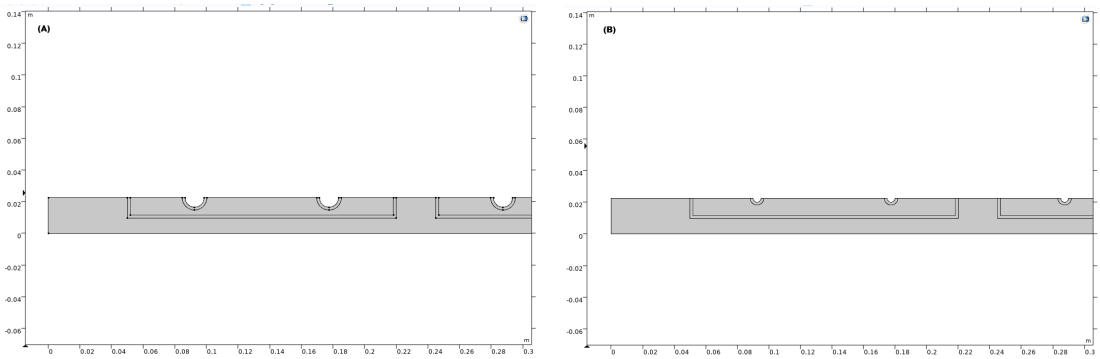

Figure 3.7: Maximum and minimum diameters for parametric investigation with hole spacing of 85 mm. (A) is $D_p = 12\ mm$ while (B) is $D_p = 5\ mm$.

Obviously, outlet temperature cannot be directly compared to the Benchmark case because of the different mass flow elaborated internally by the device. Part of the fluid passes through the auxiliary channels and the thermophysical effect is not immediately evident as **secondary channels are modelled through a boundary condition**. In the following sections this problem will be tackled by a black box 0D approach. Given the context, **water outlet temperature is used as a comparative tool to assess the effects of parameter variation on the modelled physical output of the system**.

The first sweep is done at a fixed hole spacing of 60 mm while **varying diameter**. By isolating each velocity figure 3.8 shows that for higher flow rates (A1, A2, A3) outlet temperature curves are pretty much identical. On the other hand, for A4 (minimum flow rate) there is a slight fanning of the curves with a clear (albeit negligible, in absolute terms) trend.
Higher diameters offer higher heat exchange area but at the same time cause a more pronounced striction effect. Physical water is unable to lower its temperature as much as other cases due to higher magnitude of velocity (and thus heat exchange contact time). At the same time auxiliary water extracts more energy because of a favorable skew between higher heat exchange area and smaller forced convection coefficient.

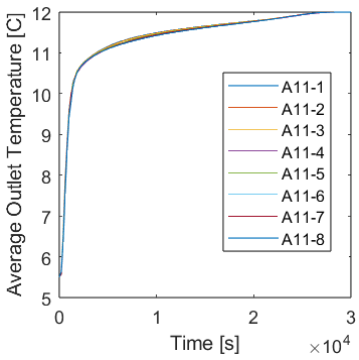

(a) Average outlet temperature for A1.

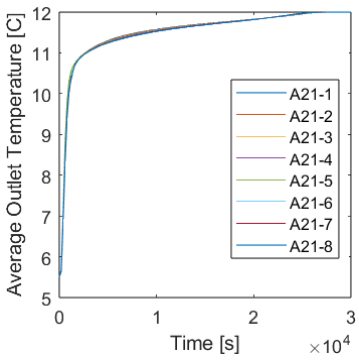

(b) Average outlet temperature for A2.

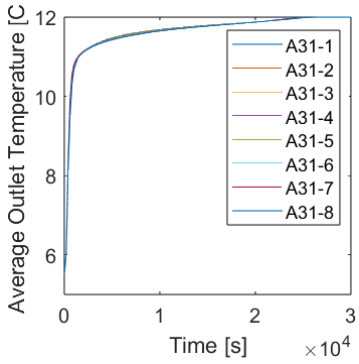

(c) Average outlet temperature for A3.

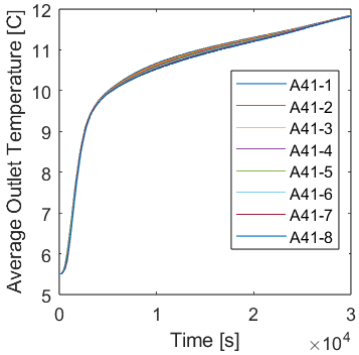

(d) Average outlet temperature for A4.

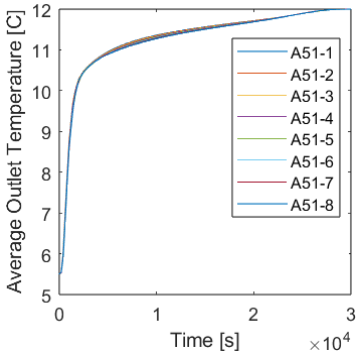

(e) Average outlet temperature for A5.

Figure 3.8: Average outlet temperature in respect to velocity groupings and diameter variations for 2 channels.

All in all, it can be concluded that **the effect of diameter on outlet temperature is negligible in this case**. As velocity decreases, the effect of geometry becomes more and more apparent. Precisely, excluding initial transient, the maximum difference in the tail end of the discharging process is 1.43% between $D_p = 12\ mm$ and $D_p = 5\ mm$ for the minimum flow rate (A4).
The conclusion is evident from τ_{80} and τ_{95} as well as visible in figure 3.10. For higher velocities (A1, A2, A3) variation between diameters is negligible but for A4 a clearer trend is visible: τ_{80} tends to increase with decreasing diameters while τ_{95} tends to decrease with smaller diameters.

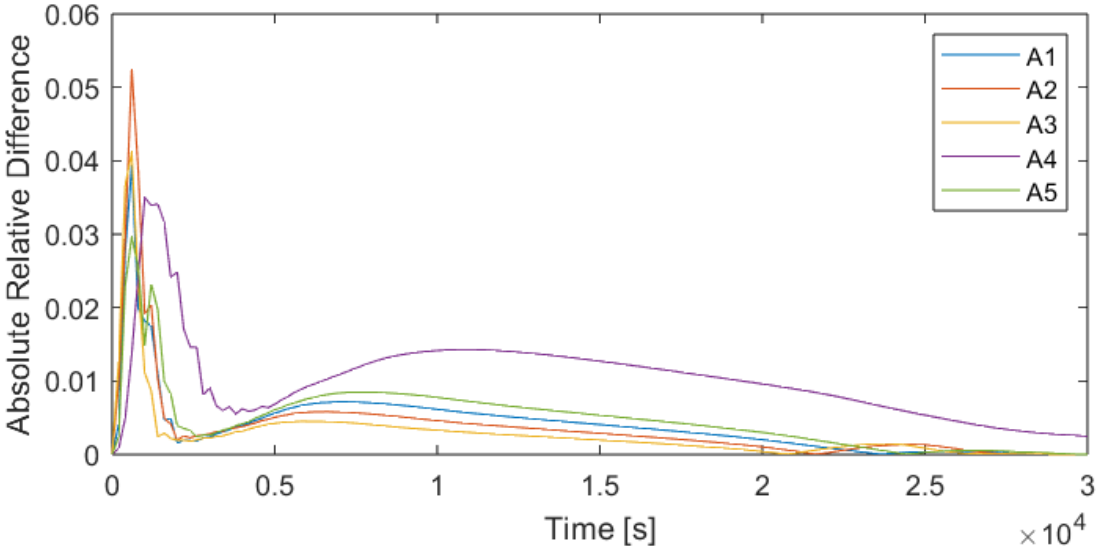

Figure 3.9: Absolute relative difference in outlet temperature between $D_p = 12\ mm$ and $D_p = 5\ mm$ for all velocities, 2 channels and 60 mm hole spacing.

For A4, the difference between τ_{80} for $D_p = 12\ mm$ against $D_p = 5\ mm$ is around 6,2% with $\tau_{80,A41-1} = 21.750s$ and $\tau_{80,A48-1} = 23.180\ s$. On the other hand the difference between τ_{95} is 2.5% with $\tau_{95,A41-1} = 28.950\ s$ and $\tau_{95,A48-1} = 29.690\ s$. KPIs based on liquid fraction can be directly compared to the benchmark device as liquid fraction is entirely simulated.

By comparing melting times for the same flow rate (A1) it can be easily seen that, despite inlet velocity being smaller, the optimized device with 2 auxiliary channels has improved the dynamic response of the system noticeably. By taking $D_p = 12\ mm$ as a reference, A41-1 achieves $\tau_{80,A41-1} = 15.960\ s$ while the benchmark case shows $\tau_{80,ref} = 17.900\ s$ with an improvement of 10.8%.

Hole spacing variation sweeps are done for 2 different diameters (12 mm and 5 mm) and 3 different spacing values (35 mm, 60 mm, 85 mm). Hole Spacing Values are reflected by the sweep IDs 1 to 3 and 4 to 6. Conversely the groups (1, 2, 3) and (4, 5, 6) relate to $D_p = 12\ mm$ and $D_p = 5\ mm$ respectively.
Results show that hole spacing does not provide any noticeable effect for $D_p = 5\ mm$ across all flow rates; the curves for water outlet are practically identical. For $D_p = 12\ mm$ at the lowest speed (A41-2, A42-2, A43-2) a trend is visible where higher hole spacing results in a slightly lower outlet temperature profile. This is due to the fact that by raising the distance the thermal pathway between the more stagnant part of the flow (around the upper part of the device, close to the top of the plates) is able to exchange heat more favorably. This ensures a more uniform distribution of energy throughout the stream even though the effect is rather negligible. Conversely by lowering the hole spacing parameter the two

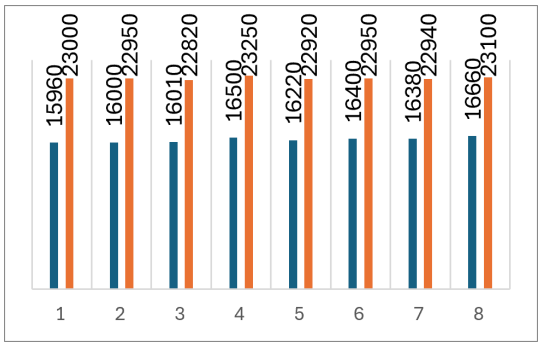

(a) Melting times for A1.

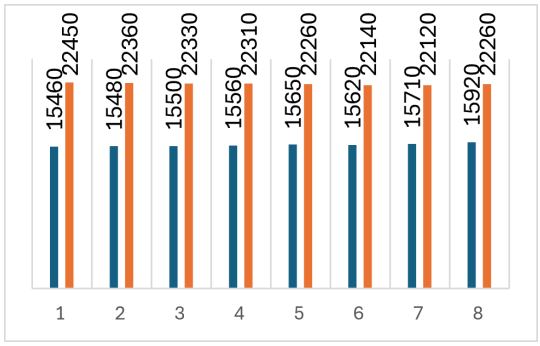

(b) Melting times for A2.

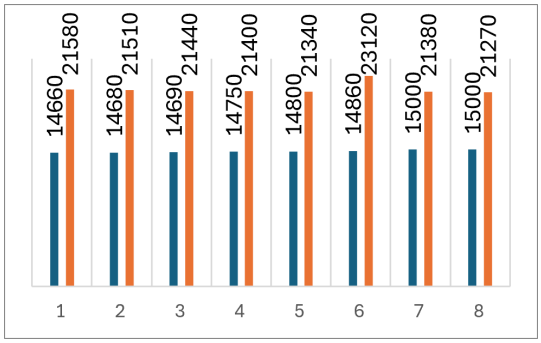

(c) Melting times for A3.

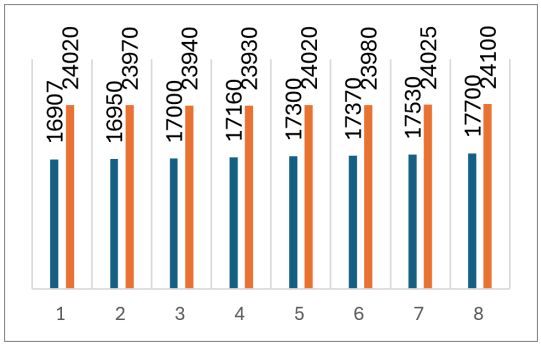

(d) Melting times for A5.

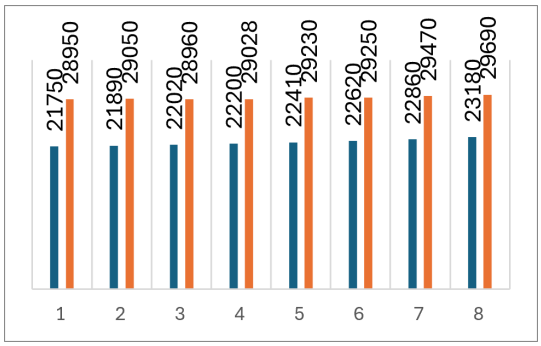

(e) Melting times for A4.

Figure 3.10: Melting times in seconds for decreasing diameters, grouped by velocity. Blue indicates τ_{80}, orange indicates τ_{95}.

hotspots are concentrated at the middle of the plate where advective transfer is maximum: since this is the main energy transport component for the problem, as seen before, results in a slightly lower outlet temperature. By miniscule variation the higher interhole spacing (which favors heat traversal to the stagnant parts of the flow) is able to harvest more energy from the physical water. Furthermore, it's possible to see how $D_p = 12\ mm$ curves are grouped upwards compared to

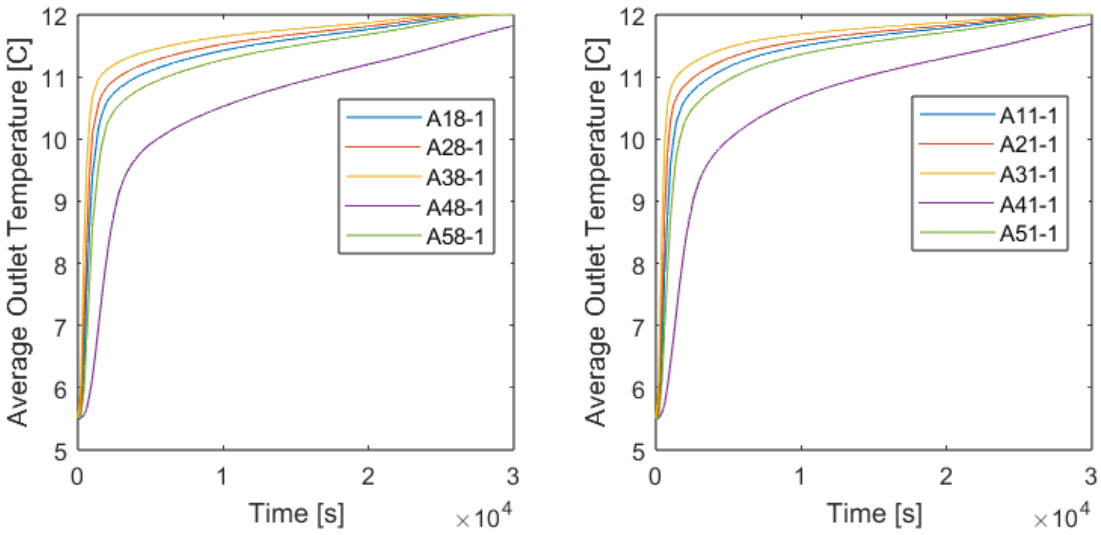

(a) Average outlet temperature for all velocities and $D_p = 5\ mm$.

(b) Average outlet temperature for all velocities and $D_p = 12\ mm$.

Figure 3.11: Comparison of outlet temperature for different velocities grouped by diameter.

$D_p = 5\ mm$ as predicted by the last sweep.

This clearly builds a hierarchy of effects which will be even more apparent later:

1. Hotspot density.
2. Advection of heat.
3. Heat exchange area and convective coefficient cross variations.
4. Heat travel pathways.

Melting times in figure 3.13 do not show any particular trend in respect to A4 and A5 (lower velocity flow rates groupings). For A2 and A3 (higher velocity groupings) on the other hand it's possible to see that for $D_p = 12\ mm$, interhole spacings of 35 mm and 85 mm have slightly improved τ_{80} melting times while no discernible trend is visible for $D_p = 5\ mm$.
Specifically, the differences amount to a maximum of 1.2% between hole spacing of 60 mm and 85 mm (respectively 14.660 s and 14480 s) showing that **the dominant effect in this case is the shortening of the heat pathway between stagnant zones and the hotspots**. The fact that the maximum difference is seen in higher speed cases is attributed to the fact that **improving heat pathways is further exploited by higher magnitude velocities**.

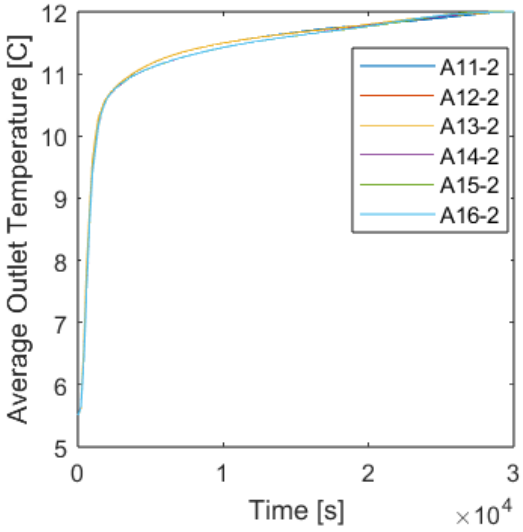

(a) Average outlet temperature for A1 and various hole spacing values.

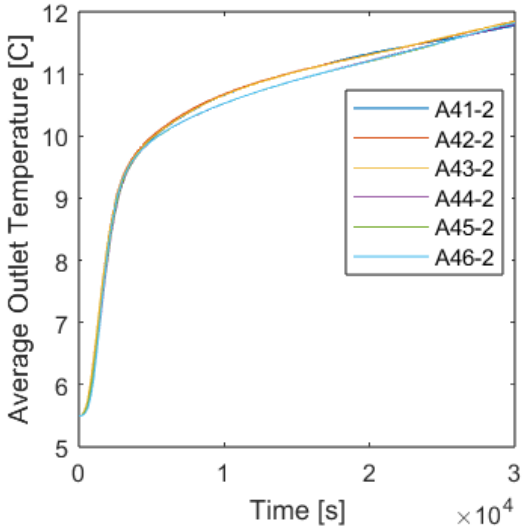

(b) Average outlet temperature for A4 and various hole spacing values.

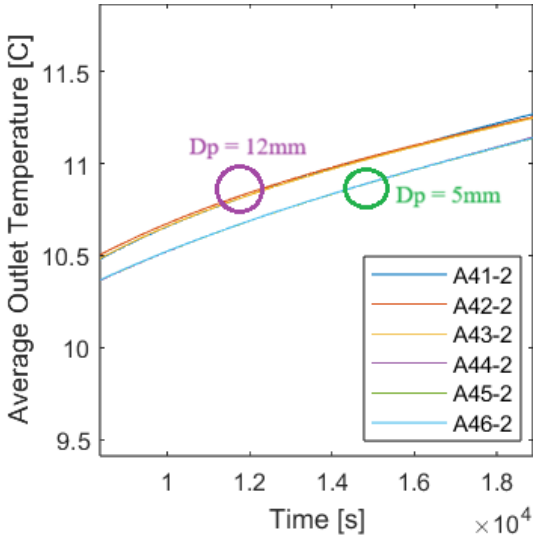

(c) Zoomed view of panel (b).

Figure 3.12: Comparison of outlet temperature for different hole spacing values grouped by velocity.

This is not visible in water outlet temperature profiles because, as discussed before, the kinematic scale takes over the diffusive scale and higher velocity diminishes total time spent by the fluid exchanging heat. While the results are intricate and varied, their effect, as mentioned in the hierarchy above, is rather negligible in absolute terms.

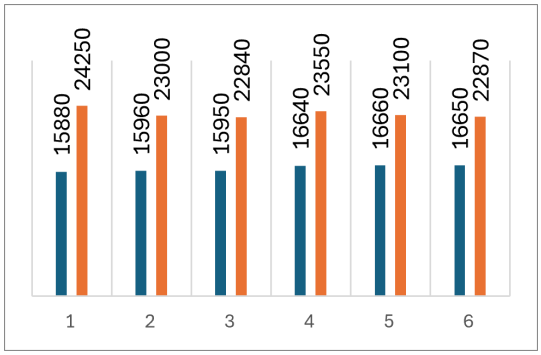

(a) Melting times for A1.

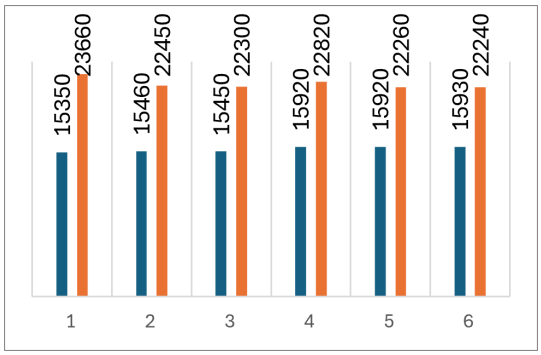

(b) Melting times for A2.

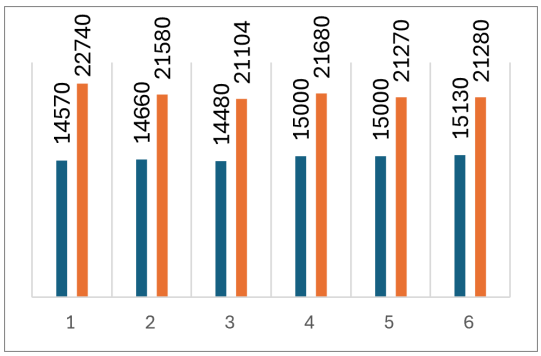

(c) Melting times for A3.

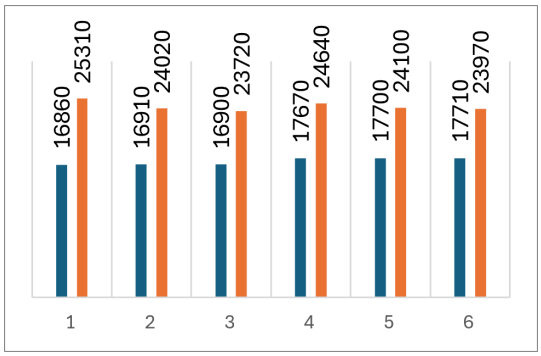

(d) Melting times for A5.

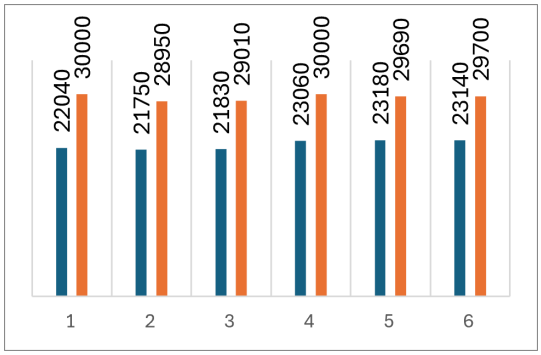

(e) Melting times for A4.

Figure 3.13: Melting times in seconds for different hole spacings and two channels, grouped by velocity. Blue indicates τ_{80}, orange indicates τ_{95}.

3 Channels - B

Results from the last suite of sweeps clearly hint at the idea that **by raising the hotspot density the system power increases noticeably**. The effect is investigated by adding one extra hotspot for a total of 3 for the B case.
The new setting consists in a similar geometry with one concentric channel for each

plate and two equally spaced channels. Hole distance for this setting refers to the distance between the central channel and each of the side channels. For this, case only 3 diameters are extracted from the previous list and studied: 12 mm, 8 mm and 5 mm. The standard hole spacing between the central channel and the two side channels for each plate is set to be 85 mm.

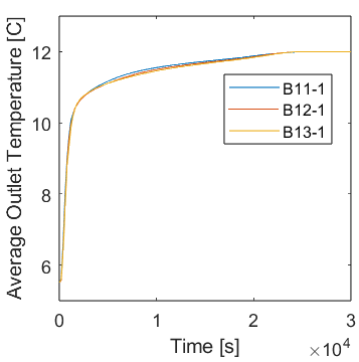

(a) Average outlet temperature for B1.

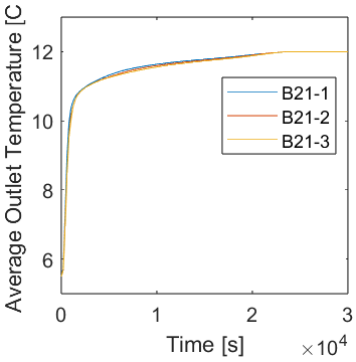

(b) Average outlet temperature for B2.

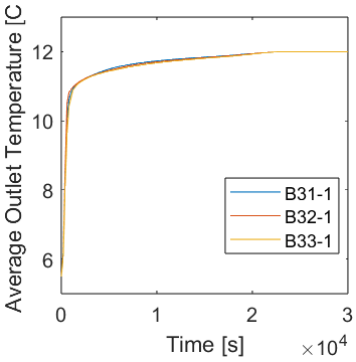

(c) Average outlet temperature for B3.

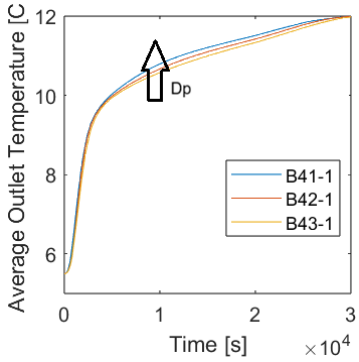

(d) Average outlet temperature for B4.

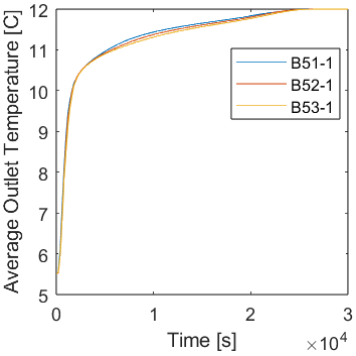

(e) Average outlet temperature for B5.

Figure 3.14: Average outlet temperature in respect to velocity groupings and diameter variations for 3 channels.

Diameter variation trends are qualitatively similar to the setup with two channels: the striction effect is much more prevalent and it is already evident at nominal inlet velocity / flow rate. Outlet temperature for B41-1, B42-1 and B43-1 shows practically identical behaviour in the initial discharging phase while around $t = 3.500\ s$ they open up. At $t = 7.000\ s$ the difference between $D_p = 12\ mm$ and $D_p = 5\ mm$ is 0.8% thus showing how the striction effect still has negligible influence on physical water outlet. The latter difference happens during the melting plateau where curves fan out and as diameter goes up so does outlet temperature.

As velocity increases the effect of geometry becomes more and more negligible with B31-1, B32-1 and B33-1 having practically overlapping water outlet curves. For the lowest velocity, on the other hand, the difference between $D_p = 12\ mm$ and $D_p = 5\ mm$ at $t = 7.000\ s$ is 1.4% and at $t = 12.600\ s$ the difference is 2.0%. This demonstrates that **while geometry effects are more prevalent at high speeds they are still rather negligible**.

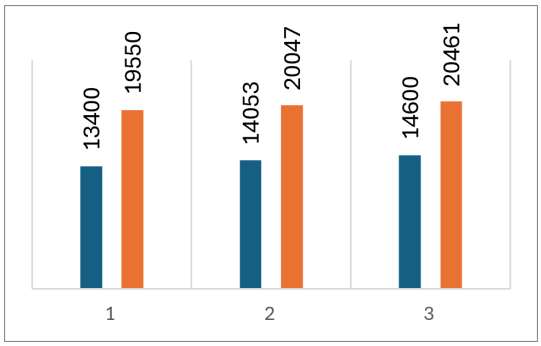

(a) Melting times for B1.

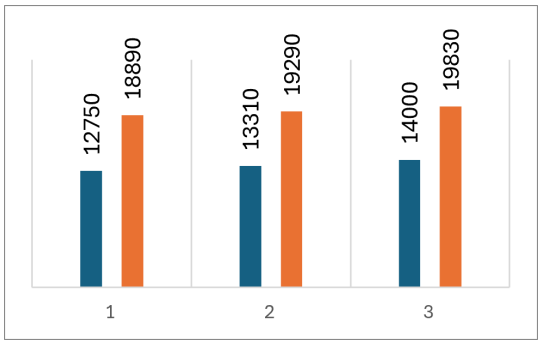

(b) Melting times for B2.

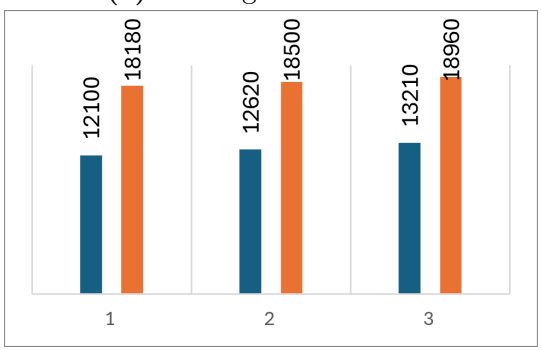

(c) Melting times for B3.

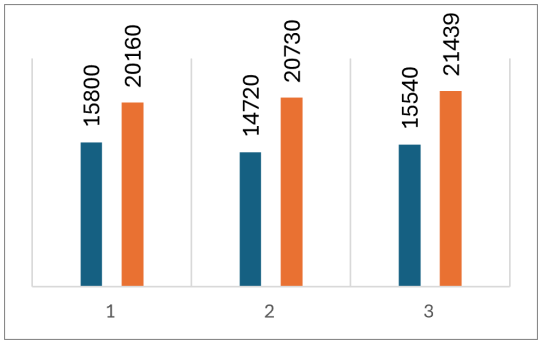

(d) Melting times for B5.

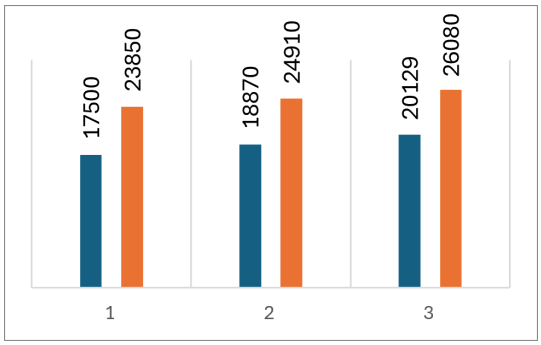

(e) Melting times for B4.

Figure 3.15: Melting times in seconds for decreasing diameters and three channels, grouped by velocity. Blue indicates τ_{80}, orange indicates τ_{95}.

Melting times exhibit a different behaviour: across each velocity $D_p = 12\ mm$ achieves the lowest melting time for both τ_{80} and τ_{95}. The trend is consistent across all diameters for each velocity sweep. B11-1 and B31-1 differ by 8.3% τ_{80} and by 4.4% on τ_{95} (respectively 13.400 s against 14.600 s and 19.550 s against 20.460 s). For the lowest velocity, as geometry takes on a more prominent role, the differences are respectively 13% and 8.6% (respectively 17.500 s against 20.130 s and 23.850 s against 26.080 s). Once again this confirms that for higher diameters, and thus higher heat exchange area, aux water absorbs more energy. As the system discharges more quickly, average power increases but the skew of energy distribution changes. This can be seen from the fact that, despite having faster melting times with $D_p = 12\ mm$, physical water is slightly hotter at the outlet.

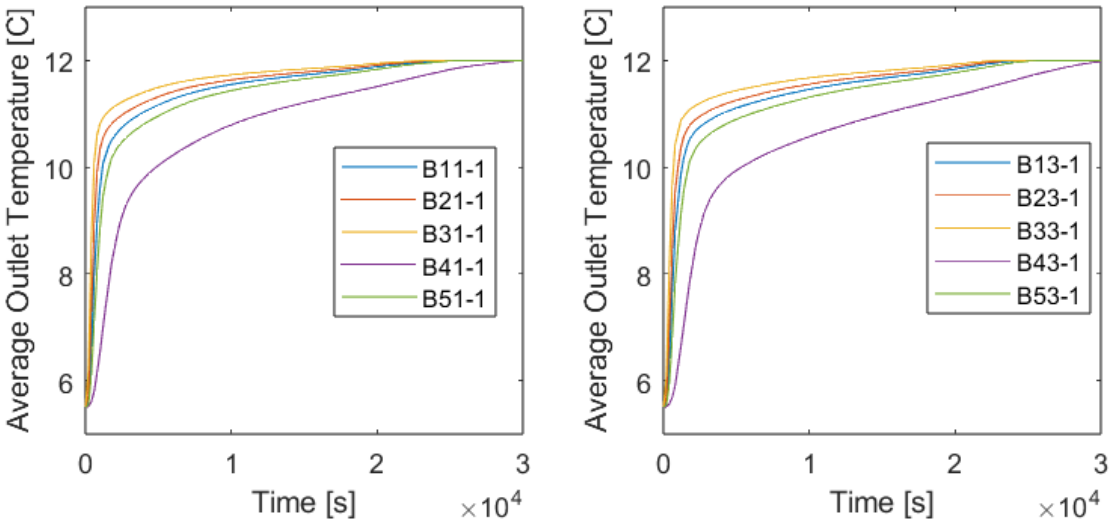

(a) Average outlet temperature for all velocities and $D_p = 12\ mm$.

(b) Average outlet temperature for all velocities and $D_p = 5\ mm$.

Figure 3.16: Comparison of outlet temperature for different velocities grouped by diameter.

Hole spacing variations are calibrated in a way that avoids extremes like the previous case. Sweeps are done for $D_p = 5\ mm$ and $D_p = 12\ mm$ for hole spacing values of 60 mm, 85 mm and 100 mm. To better explore some less visible insights, results for water outlet temperature are graphed separately for $D_p = 12\ mm$ and $D_p = 5\ mm$.

For the smallest velocity the lowest diameter achieves the best outlet temperature with hole spacing of 60 mm while in the case of nominal and higher (100 mm) hole spacings (B45-2, B46-2) water outlet temperature is practically overlapping. The same happens for $D_p = 12\ mm$ where the lowest water outlet temperature is

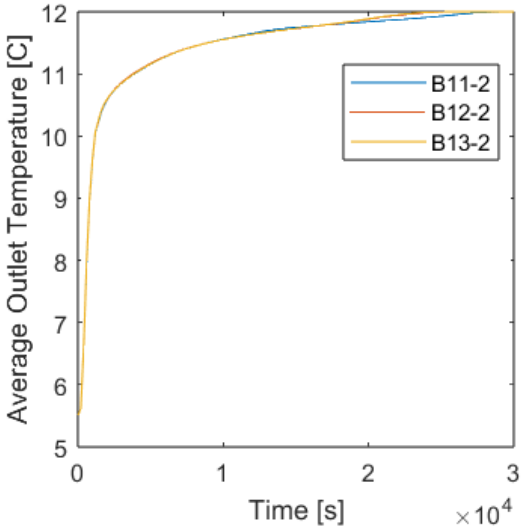

(a) Average outlet temperature for B1, increasing hole spacings and $D_p = 12\ mm$.

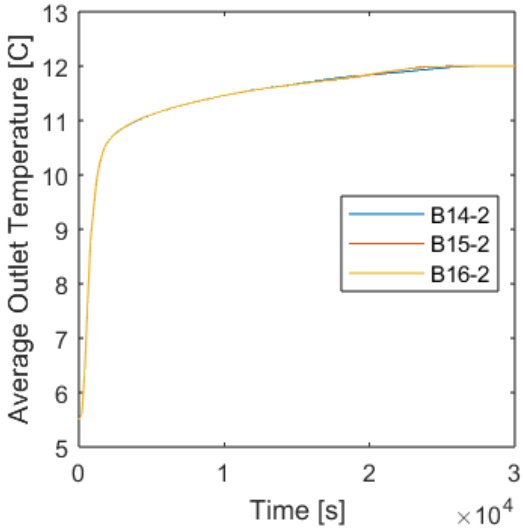

(b) Average outlet temperature for B1, increasing hole spacings and $D_p = 5\ mm$.

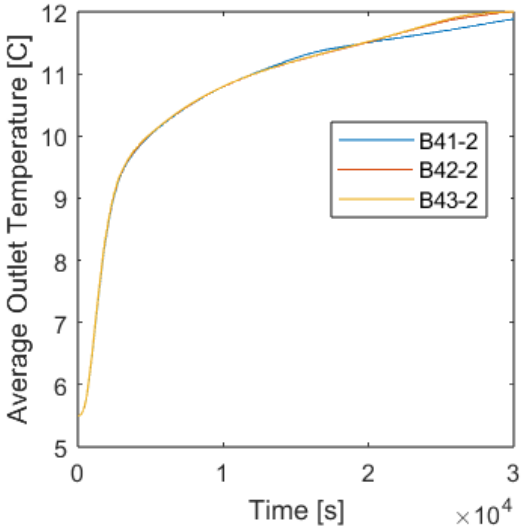

(c) Average outlet temperature for B4, increasing hole spacings and $D_p = 12\ mm$.

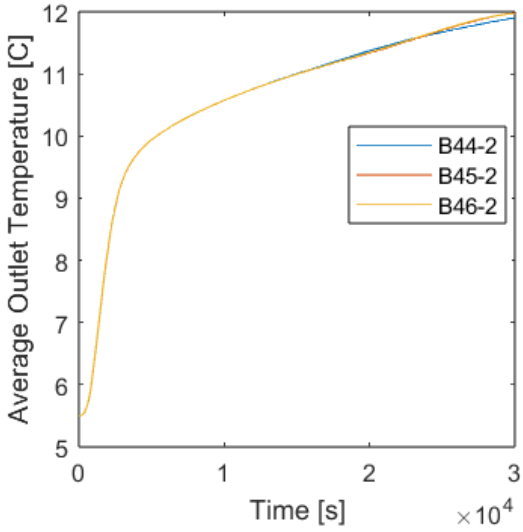

(d) Average outlet temperature for B4, increasing hole spacings and $D_p = 5\ mm$.

Figure 3.17: Average outlet temperature in respect to velocity groupings and hole spacing variations for 3 channels.

achieved in the case of 60 mm hole spacing. The latter is useful to underline that t**he outlet temperature curves practically overlap during the melting process** with B41-2 oscillating over and under B42-2 and B43-3. Between B41-2 and B42-2 the relative difference at $t = 30.000\ s$ is 0.5%. The same trends are

visible for every other velocity albeit more marginally as previously discussed.

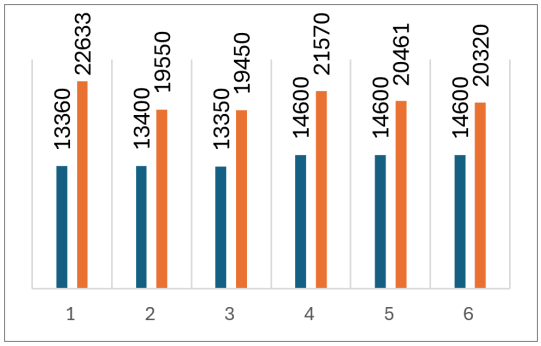

(a) Melting times for B1.

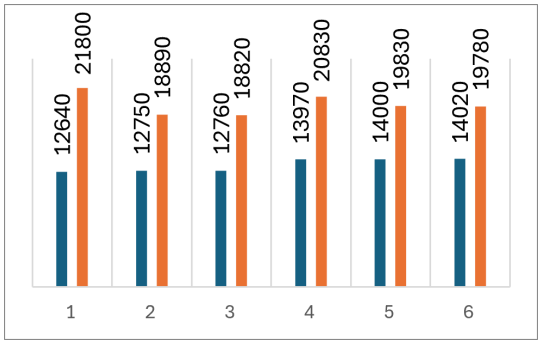

(b) Melting times for B2.

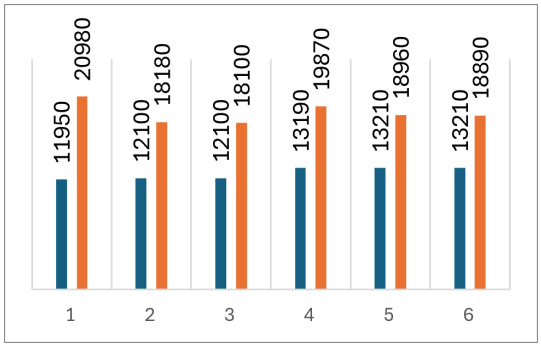

(c) Melting times for B3.

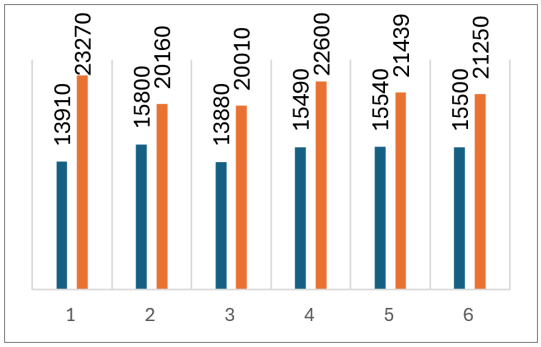

(d) Melting times for B5.

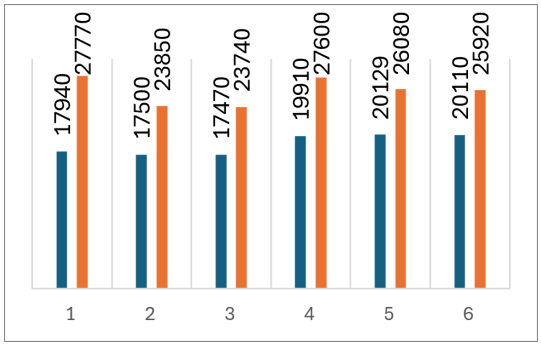

(e) Melting times for B4.

Figure 3.18: Melting times in seconds for decreasing diameters and three channels, grouped by velocity. Blue indicates τ_{80}, orange indicates τ_{95}.

Melting times on the other hand underline the critical importance of distributing hotspots evenly across plates. For every velocity and every diameter the 60 mm spacing devices show very similar τ_{80} times but exhibit noticeably higher τ_{95}. Particularly for $D_p = 12\ mm$ the maximum difference is 14% in the case of B41-2 and B42-2 while for $D_p = 5\ mm$ the maximum difference is 5.5%

between B44-2 and B45-2.
On the other hand, by a small margin, interhole spacing of 100 mm shows slightly better τ_{95} times across every velocity and every diameter with a maximum improvement of 0.9% between B56-2 and B55-2. T**he results confirm that interhole spacing is secondary to system performance but in the case of 3 auxiliary channels a more favorable setting to improve the dynamic behaviour of the system would be spacing the two auxiliary channels so as to allow them to reduce heat pathways between the more stagnant parts of water flow** while keeping the central channel for advective transport as discussed before.

Compared to the A settings, **every B setting manages lower melting time thus clearly showing a sizeable jump in system power**. By comparing the cases with $D_p = 12\ mm$ at nominal hole spacing and mass flow rate for each subset an improvement of 16.3% is achieved for τ_{80} (13.360 s vs. 15.960 s) and an improvement of 15.0% is achieved for τ_{95} (19.500 s vs 23.000 s). On the other hand for $D_p = 5\ mm$, nominal interhole spacing and nominal velocity the improvement between A and B amounts to 12.4% for τ_{80} (14.600 s vs 16.660 s) and by 12.9% for τ_{95} (20.460 s vs 23.100 s).
The jump between A and B clearly shows that by increasing the hotspot density in the plates **the system power improves noticeably** while the placement and geometry of the channels is confirmed to take on a secondary role in the context of a new set.

5 channels - C

The last suite of sweeps only includes diameter and flow rate variations as the allowable interhole distance between auxiliary channels has little possible variety.

Water outlet profiles show the same behaviour as the last cases. For $D_p = 12\ mm$ water outlet temperature is evidently higher, compared to previous settings, for each flow rate. For the lowest system velocity (C4) the difference in outlet temperature between $D_p = 12\ mm$ and $D_p = 5\ mm$ amounts to 4.0% at $t = 14.000\ s$ which is the highest seen so far. On the other hand for the highest possible velocity (C3) the difference is 1.0% at $t = 14.000\ s$. The striction effect is thus much more prominent with 5 channels. Water accelerates the most and thus advection of heat is maximized for $D_p = 12\ mm$ and minimized for $D_p = 5\ mm$. The system reacts to this change in two ways: when advection of heat is maximized the system reacts more quickly and average power increases but at the same time, given the higher speed, physical water travels much more quickly through the device reducing heat transfer time the most throughout all possible options. The latter mechanism, even if thermal power output is generally higher, makes it so that physical water stays at higher temperatures during the process.

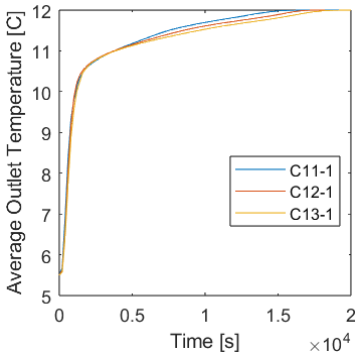

(a) Average outlet temperature for C1.

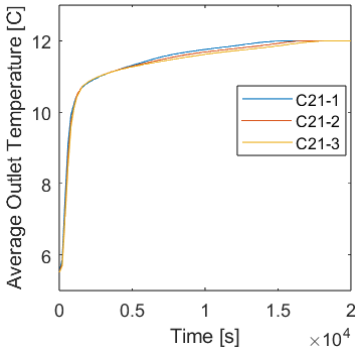

(b) Average outlet temperature for C2.

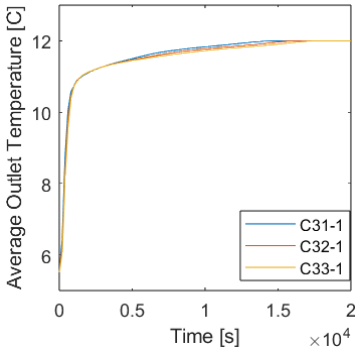

(c) Average outlet temperature for C3.

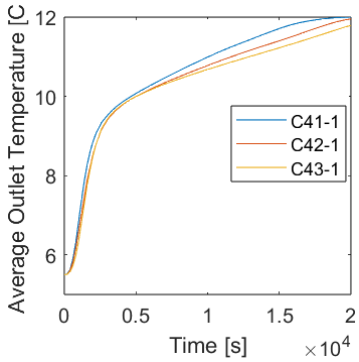

(d) Average outlet temperature for C4.

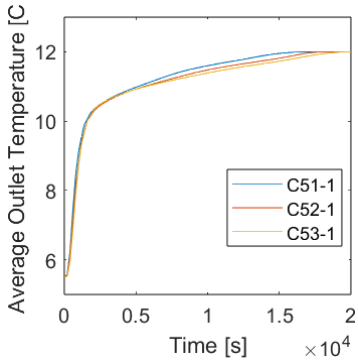

(e) Average outlet temperature for C5.

Figure 3.19: Average outlet temperature in respect to velocity groupings and diameter variations for 5 channels. Simulation time is reduced to 20.000s given the much quicker response of the system.

Melting times for nominal flow rate are the lowest among all cases with $\tau_{80} = 8.700\ s$ and $\tau_{95} = 12.240\ s$ for $D_p = 12\ mm$. Consistently with what was previously discussed, melting times for smaller diameters are higher. Results in terms of melting times compared to the B case show a 34.9% improvement for τ_{80} and 37.3% for τ_{95}. On the other hand, the comparison with the benchmark case shows an extremely promiment change: 51.4% for τ_{80} and 97.7% for τ_{95}. Interestingly, comparing results across case C itself, the difference between τ_{80} for $D_p = 12\ mm$ between maximum and minimum velocity is 30.7% and it is 22.3% for τ_{80}. The same percentage variation when considered for case A is 48.3% for τ_{80} and 34.15% for τ_{95}. This shows that case C presents a more uniform performance across different flow rates with the advantage of having a more uniform power profile with different parameters.

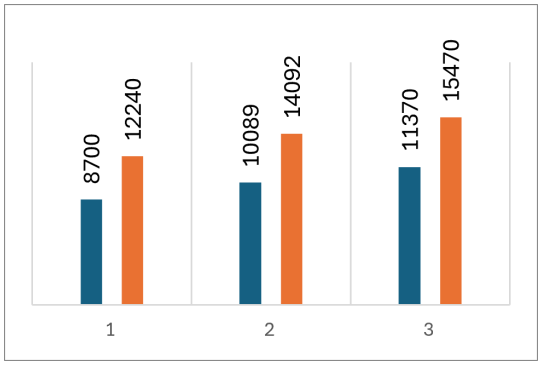

(a) Melting times for C1.

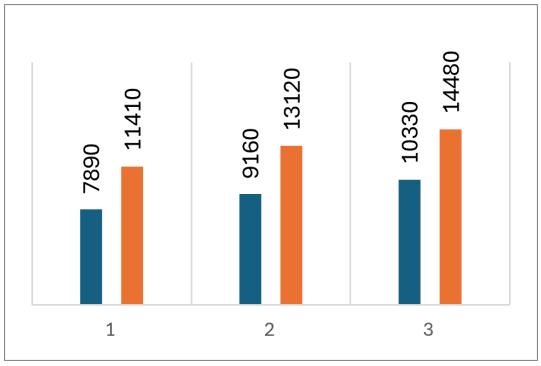

(b) Melting times for C2.

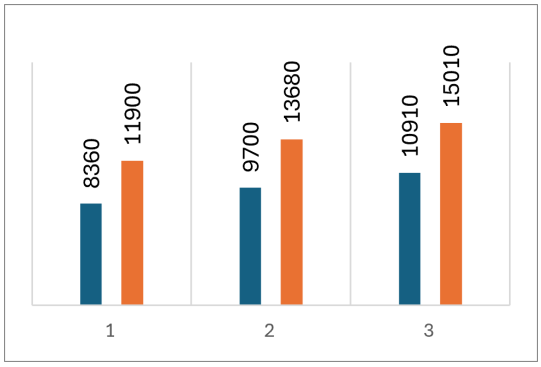

(c) Melting times for C3.

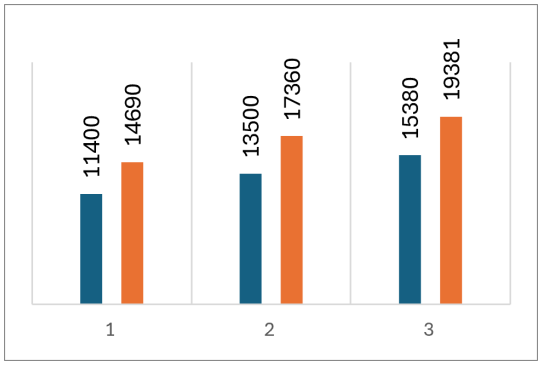

(d) Melting times for C5.

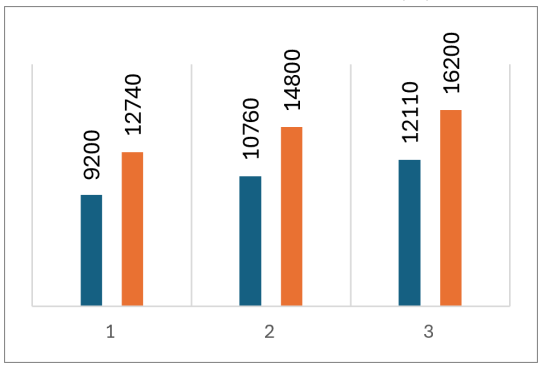

(e) Melting times for C4.

Figure 3.20: Melting times in seconds for decreasing diameters and five channels, grouped by velocity. Blue indicates τ_{80}, orange indicates τ_{95}.

In case C higher auxiliary channel diameters strongly reduce physical water outlet temperature. This will be seen for C4 velocity which, as explained before, amplifies geometry effects. By examining how energy is spread across the system it is possible

to understand precisely why this happens. This is done by plotting cumulative energy at the aux water boundaries and at the physical water boundaries separately. For $D_p = 12\ mm$ aux channel energy is always higher in absolute value compared to energy exchanged at the physical water boundary. This shows that **higher diameter (higher heat exchange area) favors higher heat exchange for aux channels**, penalizing physical water. On the other hand for $D_p = 5\ mm$ **aux water presents a higher rate of energy exchange at the beginning, crossing over at** $t = 5.000\ s$ **where physical water receives more energy compared to aux water**.
By itself, the behavior of the system in respect to diameter can't be used as a predictor, given that the model uses a surrogate boundary condition to model aux water. However, at the same time, melting time shows that higher diameter presents higher power output for 5 channels.

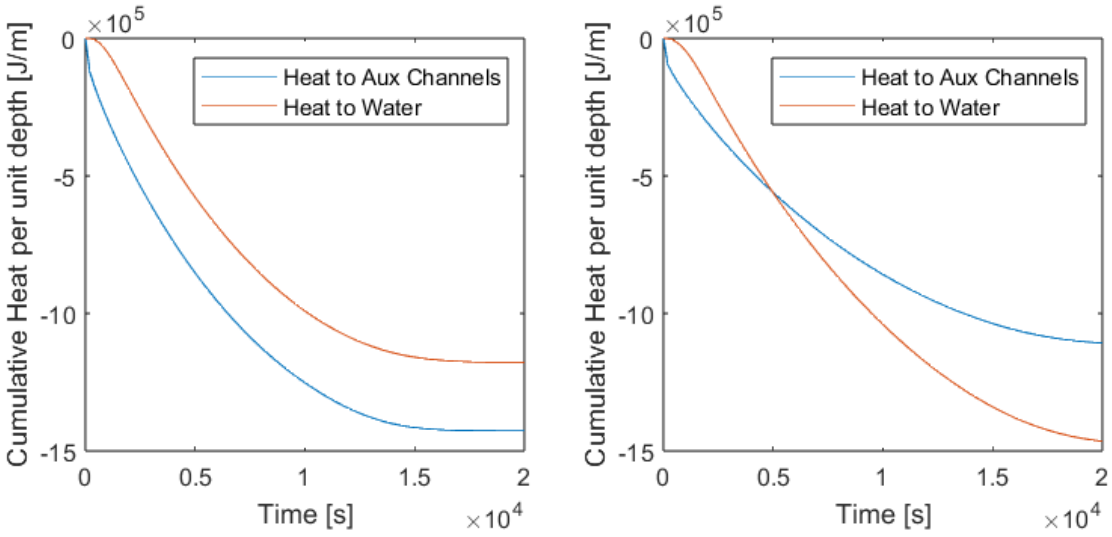

(a) Heat exchanged for $D_p = 12\ mm$. **(b)** Heat exchanged for $D_p = 5\ mm$.

Figure 3.21: Heat per unit depth exchanged at the water boundary for different diameters.

3.4.1 Energy Analysis

The PCM based thermal battery studied in this work is strongly transient. Energy analysis is used to abstract some data about power delivery in respect to melting times.
To validate the consistency of the model across all possible geometry settings, total energy output is averaged over velocity sweep suites. Simulation data shows that

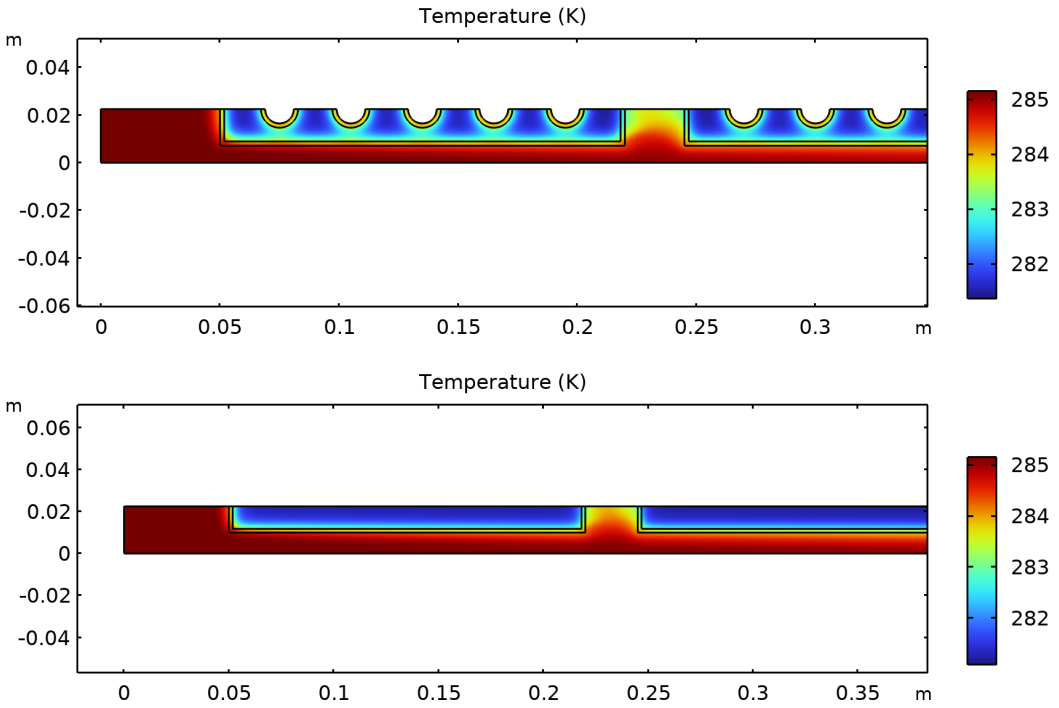

Figure 3.22: Temperature heatmaps for benchmark and five channel configurations with $D_p = 12\ mm$ at t = 2.000 s.

the highest deviation from the theoretical energy output is 2.1% for the A case. This is deemed acceptable and shows that **the model has a coherent energy closure** which makes a black-box energy analysis a great candidate to enumerate improvements obtained along each subsequent setting. For this analysis energy is obtained by calculating and integrating energy flux to physical and auxiliary water in respect to the boundary with HDPE. This ensures that the result obtained is a metric of the energy that the working fluid exchanges in respect to the device.

	0	A	B	C
Simulated energy released for 25 plates [kJ]	3020.2	2933.0	2960.2	2986.2
Theoretical energy released for 25 plates [kJ]	2995.3	2995.3	2995.3	2995.3
Percent difference	-0.83%	2.08 %	1.17 %	0.3 %

For the analysis, average power is calculated in respect to τ_{95} and τ_{80} as follows:

$$P_\tau = \frac{Q_\tau}{\tau} \tag{3.8}$$

Where Q_τ is cumulative heat exchanged at the HDPE-water boundary at $t = \tau$

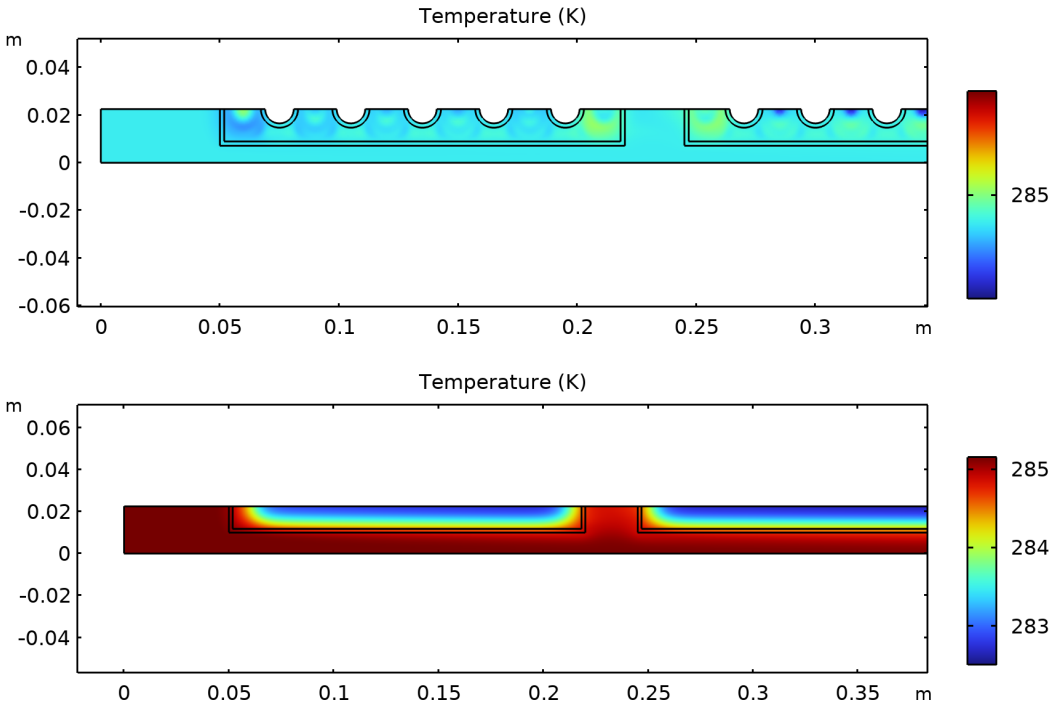

Figure 3.23: Temperature heatmaps for benchmark and five channel configurations with $D_p = 12\ mm$ at t = 15.000 s.

and τ is either τ_{95} or τ_{80}. The analysis is carried out for nominal, maximum and minimum flow-rate considering $D_p = 12\ mm$ as it has been shown to have, barring some exceptions, the lowest melting times and thus highest equivalent power.

In addition to average power it is possible to calculate an **average mixing temperature**. This is a fictitious temperature obtained by considering the system as a heat exchanger where both aux and physical water enter in a mixed state while average power is extracted. The hypothesis of having one working fluid works because both aux and physical water enter at the same temperature. Average water mixing temperature works as a black-box KPI to obtain an average outlet temperature across τ_{95} and τ_{80} independently of the fact that aux water is not directly simulated. The equation is obtained by applying the first law of thermodynamics to the ideal heat exchanger:

$$T_{out} = T_{in} - \frac{P_\tau}{\dot{m} C_p} \tag{3.9}$$

where T_{out} is the average mixing temperature, P_τ is the average power in respect to τ_{95} or τ_{80} and C_p is specific heat for water.

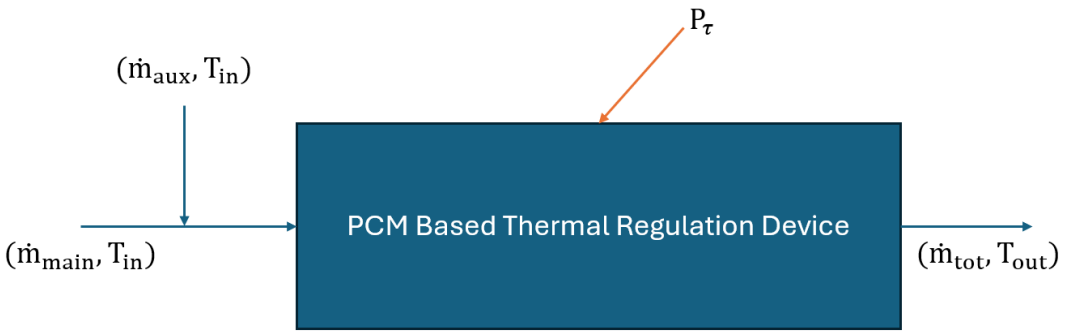

Figure 3.24: 0D Black box heat exchanger scheme.

Results confirm that there are 3 patterns:

1. Increasing the number of hotspots improves both average power and average outlet temperature.
2. Lowering flow rate decreases average power but improves outlet temperature.
3. Increasing flow rate improves average power but penalizes average outlet temperature.

Case	$\dot{m}[\frac{kg}{s}]$	τ_{95} $[s]$	$P_{\tau_{95}}$ $[kW]$	$T_{out,avg}$ $[^{\cdot}C]$
0	**0.063**	**24200**	**0.125**	**11.53**
A1	**0.063**	**23000**	**0.128**	**11.52**
A3	0.101	21580	0.136	11.68
A4	0.025	28950	0.101	11.04
B1	**0.063**	**19550**	**0.151**	**11.43**
B3	0.101	18180	0.163	11.61
B4	0.025	23850	0.124	10.83
C1	**0.063**	**12240**	**0.244**	**11.08**
C3	0.101	11410	0.262	11.38
C4	0.025	14690	0.203	10.08

For τ_{80} and nominal flow rate, cases A, B and C show average power improvements of 10.9%, 26.8% and 52.8%.
On the other hand for τ_{95} and nominal flow rate, cases A, B and C show average power improvements of 2.1%, 17.6% and 48.8%. Those results underline the fact that for the tail end of the discharging process the system tends to plateau, possibly

Case	$\dot{m}[\frac{kg}{s}]$	τ_{80} $[s]$	$P_{\tau_{80}}$ $[kW]$	$T_{out,avg}$ $[^{\cdot}C]$
0	**0.063**	**17900**	**0.143**	**11.46**
A1	**0.063**	**15960**	**0.161**	**11.39**
A3	0.101	14660	0.171	11.60
A4	0.025	21750	0.124	10.83
B1	**0.063**	**13400**	**0.196**	**11.26**
B3	0.101	12100	0.203	11.52
B4	0.025	17500	0.152	10.56
C1	**0.063**	**8700**	**0.304**	**10.85**
C3	0.101	7890	0.328	11.22
C4	0.025	11400	0.237	9.77

because of higher temperature uniformity across PCM domain at τ_{95}. At the same time case C performs noticeably better since the maximum density of hotspots ensures consistently high heat exchange.

By decreasing flow rate by 60% and considering τ_{80}, decreases in power correspond to improvements for average outlet temperature. For A a decrease in power of 23.4% corresponds to an improvement in average outlet temperature of 5.2%, for B a decrease in power of 22.4% corresponds to an improvement in average outlet temperature of 6.2% and for C a decrease in power of 22.1% corresponds to an improvement in average outlet temperature of 10.0%. This shows that by adding more hotspots to the PCM bulk the device is capable of improving energy delivery in off-design conditions with similar power delivery drops between nominal and reduced flow-rate. This is further reflected by average outlet temperature comparison between A and C for τ_{80}: setting A4 has an average outlet temperature of 10.83 °C and C4 has an average outlet temperature of 9.77 °C with a relative difference of 9.9%. In addition power difference between A4 and C4 amounts to 47.8% further compounding on the idea that adding more hotspots improves power delivery when mass advective transfer does not cap the system as discussed previously.

By increasing flow rate by 60% the device discharges more quickly at τ_{80} thus raising power while at the same time raising average mixing outlet temperature. For A an increase of power of 5.8% results in an increase of average water outlet temperature 1.8%, for B an increase of power of 3.5% results in an increase of average water outlet temperature of 2.3% and for C an increase of power of 7.3% corresponds to an increase in average water outlet temperature of 3.3%. This shows that regulating flow rate over a certain threshold, while resulting in faster melting times, decreases the average performance of the device. Hotspot density in this case shows that behaviour in respect to regulating flow upwards is not necessarily

favorable.

The last two paragraphs show that increasing hotspot density has an overall positive result for nominal and decreased flow rate while showing a decrease in performance in average water outlet temperature in exchange for faster melting times. The device thus needs to be sized conservatively in terms of flow rate because downwards regulation responds very well while upwards regulation does not offer better results. Overall increasing hotspot density shows noticeable improvements across all possible cases but upward regulation of flow rate. For upward regulation the deterioration of performance is still relatively contained compared to possible improvements showing a discrete capability of handling negative off-design conditions.

Chapter 4

Conclusions

4.1 Summary

The rapid growth of AI services and cloud computing is driving a substantial increase in data center energy consumption, making efficient thermal management an increasingly important engineering challenge. Thermal energy storage is one of the most widely adopted strategies for load management and peak demand reduction. Phase change materials (PCMs) are a common candidate to store energy in specific temperature ranges through phase change. Literature on the usage of PCM is widely available and a great range of techniques and modelling approaches for their design is well established. The usage of PCMs for data centers is thus an interesting prospect that, at the time of writing, is not well explored yet. This work focuses on one of few available papers on PCM based thermal management for data centers to explore and expand on the original idea through the development of an alternative design methodology based on distributed thermal hotspots. A 2D model is developed, validated and exploited to propose a solution based on a new optimization paradigm: "hotspot density". It consists in the addition of heat exchange hotspots for the extraction of cold energy in the most penalized parts of the PCM structure. A wide suite of parametric sweeps is conducted in order to gain insights about parameter importance and best design choices showing that hotspot density is the most prominent parameter for system performance.

4.2 Model Validation

In this work an experimental setup engineered by Liang et al. [11] was reproduced numerically by using the Enthalpy-Porosity method. The setup, consisting of 25 plates containing PCM8 (salt hydrate), is used as a cold thermal energy storage and its experimental validation hinges on a set of 3 thermocouples inserted in the

mid-bulk point of 3 consecutive plates in an elementary subchannel. By digitizing curves provided in the aforementioned paper and by obtaining simulated datapoints through COMSOL it was possible to validate the model on experimental curves provided with a maximum RMSEP of 9.85% despite the usage of a simplified two-dimensional formulation and a maximum error comparable to the thermocouple reading uncertainty indicated by Liang et al. (± 1.2 °C). Results show that even with a simplified 2D model the Enthalpy-Porosity method is a working framework capable of reproducing results obtained by other methods. Furthermore, the simulation setup is made to be energy-conservative by design through the Enthalpy-Porosity method while, for example, methods such as effective heat capacity do not grant such benefit [22]. Notably, in all cases the model closes with a maximum energy error of 2.1%. The model's behaviour is in strong agreement with the findings by Liang et al. [11] who also underline the importance of flow rate and plate height. On the other hand this work expanded on secondary order effects in the framework of an optimization protocol confirming the findings from Liang et al. about the key design parameters. These results indicate that the Enthalpy-Porosity formulation successfully captures the dominant heat transfer mechanisms governing the discharge process. This result clearly communicates the robustness of the model as it converges to the same results found by Liang et al. with another numerical framework. Globally the model behaves rather accurately. However, challenges are posed to the accuracy of the late melting process where temperature behaviour of plates tends to "overshoot" compared to experimental data: this is attributed to 2D simplification which does not capture the skew of volume to surface ratio that often results in more complex heat exchange dynamics.

4.3 Optimization Results

An optimization method based on adding hotspots to the PCM bulk is proposed. It works as a crossflow heat exchanger with two perpendicular working fluid directions that are hydraulically separate. The method was developed with material constraints that make the usage of more common solutions found in literature difficult to adopt. The 2D model developed was adapted with a new geometry and a surrogate Robin boundary condition in order to obtain proof of concept evaluation.
Results show that the primary driver is **hotspot density**: adding more auxiliary channels (2 to 5) consistently increases power and improves average outlet temperature. The "best case" with 5 auxiliary channels shows that there is great improvement over the reference case (51.4%) in the system's initial response in terms of τ_{80}. This is also notable with a strong resolution of the late melting plateau with a 97.7% improvement over τ_{95}. Furthermore, the 5 channels solution allows the

best off-design regulation of the system with much lower differences in τ_{80} between different flow rate regimes. This is also reflected in the energy analysis chapter where it is shown that with a comparable drop in power due to the decrease in flow rate the 5 channels setting achieves the best improvement with case A showing an improvement of 5.4% while case C shows a nearly doubled improvement of 10% thus making better use of the same resources in terms of power delivery. On the other hand the system does not scale as well with upwards regulation with the 5 channels setup showing a slightly worse drop in power compared to the 2 and 3 channels solution.
Geometry tweaks to the setup were shown to have secondary order effects. The case with 2 auxiliary channels is taken as the example as fluid acceleration due to plate height variation is minimal. Diameter variation effect is negligible overall with the minimum flow rate showing a maximum difference in outlet temperature of 2.0%. The same can be said about the hole spacing parameter where the difference is even smaller compared to variation in diameter and the only effect is a minor variation in heat distribution pathways that does not strongly affect system performance.
The hierarchy defined in chapter 3 is thus confirmed across all device settings, the relative importance of hotspot density is highest with flow rate coming second, plate height and diameter third and then hole spacing. This is in agreement with Liang et al. who also found that flow rate and plate height (which influences velocity) are key parameters. Conclusions drawn from this study show that improvement is consistent along the board when more auxiliary channels are added and in general the idea of independent hotspots strongly improves performance even around geometrical parameter variations.

4.4 Limitations and Future Work

The model presented in this work while satisfactory for a preliminary analysis still presents some critical challenges. Natural convection is an important part of modelling PCM based thermal batteries, while not a defining factor added insights from gravity driven buoyancy flows may slightly alter results. Modelling of auxiliary channels is done in a way that ensures energy conservation and coherency but direct simulation of secondary channels is necessary to ensure expected behaviour. In this work an assumption was made about the Nusselt number for aux water to consider that choice but a 3D model or a 2D + 1D solution would return more precise insights about aux water. Variation of parameters such as density (specific volume) were not considered. For the chosen PCM density variation is noticeable and in conjunction with buoyancy driven flows may noticeably alter results. A finer analysis of thermal contacts due to volume change of PCM during solidification in the manufacturing process is another neglected part of the model that for future

work may improve physical adherence of the model.
On the other hand the model's greatest strength is its computational simplicity. The characterization of a transfer function for outlet temperature may easily be done given that subsequent simulations are extremely quick. It would encompass different boundary condition cases which were not taken into account in this work. Transfer functions could be done for a variety of geometrical subsets which may then be used to compare performance in the broader spectrum of a thermo-electrical network. Inversely, the development of a 3D model in the future may help to further understand finer details about heat distribution and flow stagnation to propose radically different geometries. The usage of topology optimization for aux water channels is another interesting prospect to optimize the channel shape to better distribute "hotspot surface".
In this work the charging process was omitted, given that charging behaviour often differs and different insights may be gained, future work focusing on the duality of charging and discharging is a favorable prospect.

4.5 Conclusive Remarks

Cooling load is one of the main components in energy consumption for data centers which, according to IEA, is projected to grow exponentially over the following years. This work proposed a novel and computationally lean approach in the design of a thermal battery solution to aid in the regulation of thermal subsystems in peak or emergency conditions. The proposed solution, while being a proof of concept, provides a promising foundation into subsequent studies at both system level (0D approach for thermal networks) and component level (3D model). Overall, the results demonstrate that the introduction of distributed thermal hotspots constitutes a promising design strategy for PCM based thermal batteries. While further validation and higher-fidelity modelling are required, the proposed approach consistently improves discharge performance and provides a viable foundation for future developments in data-center thermal energy storage systems.

List of Figures

Acknowledgements

To my mother and my father.

To Fabrizio and Ermanno.

To Nikolai.

To Fra l'altro, Vecchia, Conti, Stefano, Valentina and Momo.

Across the world, to Serena.

To people of the past with whom different directions were taken.

To my present and hopefully my future.

To Anita and Alice.

To my supervisor E. Chiavazzo for making this thesis possible.

Special thanks to my co-supervisor M. Morciano for the invaluable help and availability all throughout the project.

Last but not least to Rebecca for running an obscene amount of simulations without catching on fire.

Bibliography

[1] Matteo Morciano, Matteo Fasano, Eliodoro Chiavazzo, and Luigi Mongibello. «Trending applications of Phase Change Materials in sustainable thermal engineering: An up-to-date review». In: *Energy Conversion and Management: X* 25 (2025), p. 100862. ISSN: 2590-1745. DOI: https://doi.org/10.1016/j.ecmx.2024.100862. URL: https://www.sciencedirect.com/science/article/pii/S2590174524003404 (cit. on pp. 1, 3, 4).

[2] Atul Kumar, Ashok Kumar Dewangan, and Ashok Kumar Yadav. «A state-of-the-art review on modelling and simulation of battery thermal management system using phase change material and liquid cooling: Enhancing performance, sustainability, and future research needs». In: *Journal of Energy Storage* 133 (2025), p. 117978. ISSN: 2352-152X. DOI: https://doi.org/10.1016/j.est.2025.117978. URL: https://www.sciencedirect.com/science/article/pii/S2352152X2502691X (cit. on pp. 1, 3).

[3] M. Moreira, T. Silva, J. Dias-de-Oliveira, F. Neto, and C. Amaral. «Numerical modelling of radiant systems and phase change materials in building applications - a review». In: *Applied Thermal Engineering* 234 (2023), p. 121342. ISSN: 1359-4311. DOI: https://doi.org/10.1016/j.applthermaleng.2023.121342. URL: https://www.sciencedirect.com/science/article/pii/S1359431123013716 (cit. on pp. 1, 17).

[4] Chongmao Mo, Jiekai Xie, Guoqing Zhang, Zhiyang Zou, and Xiaoqing Yang. «All-climate battery thermal management system integrating units-assembled phase change material module with forced air convection». In: *Energy* 294 (2024), p. 130642. ISSN: 0360-5442. DOI: https://doi.org/10.1016/j.energy.2024.130642. URL: https://www.sciencedirect.com/science/article/pii/S0360544224004146 (cit. on p. 1).

[5] Xin Ge, Xinxi Li, Yang Jin, Guoqing Zhang, Jian Deng, and Jianfang Ge. «Experimental investigation on thermal management system of composite phase change material coupled with serpentine tubes for battery module». In: *Applied Thermal Engineering* 219 (2023), p. 119501. ISSN: 1359-4311. DOI: https://doi.org/10.1016/j.applthermaleng.2022.119501. URL: https:

//www.sciencedirect.com/science/article/pii/S1359431122014314 (cit. on p. 2).

[6] Guanyi Chen, Yong Shi, Hanyang Ye, and Hang Kang. «Experimental study on phase change material based thermal management design with adjustable fins for lithium-ion battery». In: *Applied Thermal Engineering* 221 (2023), p. 119808. ISSN: 1359-4311. DOI: https://doi.org/10.1016/j.applthermaleng.2022.119808. URL: https://www.sciencedirect.com/science/article/pii/S1359431122017380 (cit. on p. 2).

[7] Jie Mei, Guoqing Shi, He Liu, Zhi Wang, and Mingyi Chen. «Investigation on the optimization strategy of phase change material thermal management system for lithium-ion battery». In: *Journal of Energy Storage* 55 (2022), p. 105365. ISSN: 2352-152X. DOI: https://doi.org/10.1016/j.est.2022.105365. URL: https://www.sciencedirect.com/science/article/pii/S2352152X22013597 (cit. on p. 2).

[8] Bin Huang, Ziao Zheng, Gaofeng Lu, and Xiaoqiang Zhai. «Design and experimental investigation of a PCM based cooling storage unit for emergency cooling in data center». In: *Energy and Buildings* 259 (2022), p. 111871. ISSN: 0378-7788. DOI: https://doi.org/10.1016/j.enbuild.2022.111871. URL: https://www.sciencedirect.com/science/article/pii/S0378778822000421 (cit. on pp. 3, 10, 11).

[9] Suraj Rana, Rajan Kumar, and Rabinder Singh Bharj. «Experimental and numerical investigation on the thermal performance of fin-enhanced PCM-based temperature regulation system for lithium-ion batteries». In: *International Journal of Thermal Sciences* 220 (2026), p. 110311. ISSN: 1290-0729. DOI: https://doi.org/10.1016/j.ijthermalsci.2025.110311. URL: https://www.sciencedirect.com/science/article/pii/S1290072925006349 (cit. on pp. 3, 4).

[10] W. Youssef, Y.T. Ge, and S.A. Tassou. «CFD modelling development and experimental validation of a phase change material (PCM) heat exchanger with spiral-wired tubes». In: *Energy Conversion and Management* 157 (2018), pp. 498–510. ISSN: 0196-8904. DOI: https://doi.org/10.1016/j.enconman.2017.12.036. URL: https://www.sciencedirect.com/science/article/pii/S0196890417311871 (cit. on p. 3).

[11] Yan Liang, Haibin Yang, Huilong Wang, Xiaohua Bao, and Hongzhi Cui. «Enhancing energy efficiency of air conditioning system through optimization of PCM-based cold energy storage tank: A data center case study». In: *Energy* 286 (2024), p. 129641. ISSN: 0360-5442. DOI: https://doi.org/10.1016/j.energy.2023.129641. URL: https://www.sciencedirect.com/science/

article/pii/S0360544223030359 (cit. on pp. 3, 11, 12, 14, 15, 22, 24, 30, 35, 62, 63).

[12] Jianjuan Yuan, Yuyao Yan, Xuemei Zhang, Xiangfei Kong, and Tao Zhang. «Coupling of flexible phase change materials and servers for improving the security of data centers in emergency situations». In: *Applied Thermal Engineering* 242 (2024), p. 122439. ISSN: 1359-4311. DOI: https://doi.org/10.1016/j.applthermaleng.2024.122439. URL: https://www.sciencedirect.com/science/article/pii/S1359431124001078 (cit. on pp. 3, 4, 10).

[13] Priti D. Dhabarde, Rajendra Prasad Soni, and Jiwak G. Suryawanshi. «Passive-cooling of Li-ion batteries using PCM-metal foam in honeycomb enclosure». In: *Applied Thermal Engineering* 281 (2025), p. 128543. ISSN: 1359-4311. DOI: https://doi.org/10.1016/j.applthermaleng.2025.128543. URL: https://www.sciencedirect.com/science/article/pii/S1359431125031357 (cit. on p. 3).

[14] Nilesh Krishnadhari Singh and Rashmi Rekha Sahoo. «Rayleigh-Bénard performance effect on battery cooling using CPCM with novel fin configuration». In: *Thermal Science and Engineering Progress* 65 (2025), p. 103929. ISSN: 2451-9049. DOI: https://doi.org/10.1016/j.tsep.2025.103929. URL: https://www.sciencedirect.com/science/article/pii/S2451904925007206 (cit. on pp. 3, 5, 6).

[15] Sahin Gungor and Sylvie Lorente. «PCM-based passive cooling solution for Li-ion battery pack, a theoretical and numerical study». In: *Applied Thermal Engineering* 257 (2024), p. 124262. ISSN: 1359-4311. DOI: https://doi.org/10.1016/j.applthermaleng.2024.124262. URL: https://www.sciencedirect.com/science/article/pii/S1359431124019306 (cit. on p. 3).

[16] Houssein Ammar, Mahdi Delbani, Farouk Fardoun, Bassem El Zoghbi, Hussein Mouzanar, Jalal Faraj, and Mahmoud Khaled. «Hybrid liquid–PCM thermal management for high–capacity lithium–ion batteries under fast charging: A parametric comparative study». In: *Results in Engineering* 27 (2025), p. 106674. ISSN: 2590-1230. DOI: https://doi.org/10.1016/j.rineng.2025.106674. URL: https://www.sciencedirect.com/science/article/pii/S2590123025027410 (cit. on pp. 4, 5).

[17] Abubakar Gambo Mohammed, Hasril Hasini, Karem Elsayed Elfeky, Mutari Hajara Ali, and Nur Irmawati Om. «Enhanced thermal regulation of Li-ion batteries for rapid charge-discharge application using metallic PCM». In: *Case Studies in Thermal Engineering* 74 (2025), p. 106901. ISSN: 2214-157X. DOI: https://doi.org/10.1016/j.csite.2025.106901. URL: https:

//www.sciencedirect.com/science/article/pii/S2214157X2501161X (cit. on pp. 4, 30).

[18] Ahmed Saad Soliman, Ali Radwan, Mohamed Samir Fouda, and Ping Cheng. «A novel heat sink for thermal management of lithium-ion battery with hybrid air convection and fins filled with multiple PCMs». In: *Applied Thermal Engineering* 279 (2025), p. 127841. ISSN: 1359-4311. DOI: https://doi.org/10.1016/j.applthermaleng.2025.127841. URL: https://www.sciencedirect.com/science/article/pii/S1359431125024330 (cit. on p. 5).

[19] Huafu Chen, Gaosheng Wei, Li Xu, and Xiaoze Du. «Performance study on a novel hybrid thermal management system for cylindrical lithium-ion battery pack based on liquid cooling and PCM». In: *Applied Thermal Engineering* 271 (2025), p. 126392. ISSN: 1359-4311. DOI: https://doi.org/10.1016/j.applthermaleng.2025.126392. URL: https://www.sciencedirect.com/science/article/pii/S1359431125009846 (cit. on pp. 5, 36).

[20] Wei Sun, Peng Li, Wenmin Cheng, Chongchong Li, Xiaolong Qi, Han Shen, and Xiaodong Shao. «Novel hybrid thermal management system for cylindrical lithium-ion battery based on CPCM and topology-optimized liquid cooling». In: *Energy* 329 (2025), p. 136719. ISSN: 0360-5442. DOI: https://doi.org/10.1016/j.energy.2025.136719. URL: https://www.sciencedirect.com/science/article/pii/S0360544225023618 (cit. on pp. 6, 7).

[21] Myrto Zeneli, Aris Nikolopoulos, Sotirios Karellas, and Nikolaos Nikolopoulos. «Chapter 7 - Numerical methods for solid-liquid phase-change problems». In: *Ultra-High Temperature Thermal Energy Storage, Transfer and Conversion*. Ed. by Alejandro Datas. Woodhead Publishing Series in Energy. Woodhead Publishing, 2021, pp. 165–199. ISBN: 978-0-12-819955-8. DOI: https://doi.org/10.1016/B978-0-12-819955-8.00007-7. URL: https://www.sciencedirect.com/science/article/pii/B9780128199558000077 (cit. on pp. 6, 12, 19, 20).

[22] G. Ziskind. «12 - Modelling of heat transfer in phase change materials (PCMs) for thermal energy storage systems». In: *Advances in Thermal Energy Storage Systems*. Ed. by Luisa F. Cabeza. Woodhead Publishing Series in Energy. Woodhead Publishing, 2015, pp. 307–324. ISBN: 978-1-78242-088-0. DOI: https://doi.org/10.1533/9781782420965.2.307. URL: https://www.sciencedirect.com/science/article/pii/B9781782420880500122 (cit. on pp. 6, 63).

[23] Zaid Ahmed Belwadi and Rajesh Akula. «Design of a PCM-based thermal management system for cylindrical Li-ion battery using topology optimization». In: *Applied Thermal Engineering* 270 (2025), p. 126143. ISSN: 1359-4311. DOI:

https://doi.org/10.1016/j.applthermaleng.2025.126143. URL: https://www.sciencedirect.com/science/article/pii/S1359431125007355 (cit. on p. 7).

[24] Alex de Vries-Gao. «The carbon and water footprints of data centers and what this could mean for artificial intelligence». In: *Patterns* 7.1 (2026), p. 101430. ISSN: 2666-3899. DOI: https://doi.org/10.1016/j.patter.2025.101430. URL: https://www.sciencedirect.com/science/article/pii/S2666389925002788 (cit. on p. 7).

[25] Ali Khosravi, Oscar R. Sandoval, Melika Sadat Taslimi, Tiia Sahrakorpi, Gessica Amorim, and Juan Jose Garcia Pabon. «Review of energy efficiency and technological advancements in data center power systems». In: *Energy and Buildings* 323 (2024), p. 114834. ISSN: 0378-7788. DOI: https://doi.org/10.1016/j.enbuild.2024.114834. URL: https://www.sciencedirect.com/science/article/pii/S0378778824009502 (cit. on p. 7).

[26] Jinsoo Kim et al. «Reviewing the socio-technical dynamics of AI, data centers and digitalization on energy and the environment». In: *Renewable and Sustainable Energy Reviews* 234 (2026), p. 116861. ISSN: 1364-0321. DOI: https://doi.org/10.1016/j.rser.2026.116861. URL: https://www.sciencedirect.com/science/article/pii/S1364032126001607 (cit. on pp. 7, 8).

[27] Amit Kumar and Naran M. Pindoriya. «Toward sustainable data center operation: A review on existing infrastructures, integrated smart energy management frameworks, and future perspectives». In: *Renewable and Sustainable Energy Reviews* 230 (2026), p. 116664. ISSN: 1364-0321. DOI: https://doi.org/10.1016/j.rser.2025.116664. URL: https://www.sciencedirect.com/science/article/pii/S1364032125013371 (cit. on pp. 8–10).

[28] Xiaolei Yuan, Xuetao Zhou, Yiqun Pan, Risto Kosonen, Hao Cai, Yang Gao, and Yu Wang. «Phase change cooling in data centers: A review». In: *Energy and Buildings* 236 (2021), p. 110764. ISSN: 0378-7788. DOI: https://doi.org/10.1016/j.enbuild.2021.110764. URL: https://www.sciencedirect.com/science/article/pii/S0378778821000487 (cit. on pp. 8, 9).

[29] Biruk Agegnehu, Karl Liebezeit, Matteo Fasano, Matteo Morciano, and Eliodoro Chiavazzo. «Dynamic PCM for high-performance latent thermal energy storage: A numerical and parametric study». In: *International Communications in Heat and Mass Transfer* 167 (2025), p. 109277. ISSN: 0735-1933. DOI: https://doi.org/10.1016/j.icheatmasstransfer.2025.109277. URL: https://www.sciencedirect.com/science/article/pii/S0735193325007031 (cit. on p. 20).

[30] *RT10HC Techdata*. URL: https://www.rubitherm.eu/media/products/datasheets/Techdata_-RT10HC_EN_11032024.PDF (cit. on p. 31).

[31] Amr Rabiea and Taher Halawa. «Investigation of the effect of eccentricity and shell diameter on the charging performance of erythritol for thermal energy storage». In: *Case Studies in Thermal Engineering* 65 (2025), p. 105648. ISSN: 2214-157X. DOI: https://doi.org/10.1016/j.csite.2024.105648. URL: https://www.sciencedirect.com/science/article/pii/S2214157X24016794 (cit. on p. 36).

[32] Nidhal Ben Khedher, Khashayar Hosseinzadeh, Azher M. Abed, Koorosh Khosravi, Jasim M. Mahdi, Hakim S. Sultan, Hayder I. Mohammed, and Pouyan Talebizadehsardari. «Accelerated charging of PCM in coil heat exchangers via central return tube and inlet positioning: A 3D analysis». In: *International Communications in Heat and Mass Transfer* 152 (2024), p. 107275. ISSN: 0735-1933. DOI: https://doi.org/10.1016/j.icheatmasstransfer.2024.107275. URL: https://www.sciencedirect.com/science/article/pii/S073519332400037X (cit. on pp. 36, 37).